International Journal of
Molecular Sciences

MDPI

Article

Network Pharmacology, Molecular Modeling, and Surface Plasmon Resonance Combined with In Vitro Validation to Elucidate the Anti-Inflammatory Effects of Delphinidin in LPS-Stimulated Macrophages: Potential Relevance to Vascular Disease

Yiqian Zhang [1], Lingran Feng [2], Haomin Li [1], Long Yao [1], Tingxuan Zheng [2], Sihan Jia [1] and Dongmei Yang [1,*]

[1] Medical School, Hunan University of Chinese Medicine, Changsha 410208, China
[2] School of Integrated Chinese and Western Medicine, Hunan University of Chinese Medicine, Changsha 410208, China
* Correspondence: dongmeiy@hnucm.edu.cn

Abstract

Macrophage-driven inflammation is an important contributor to the development and progression of chronic vascular diseases. Although statins substantially reduce cardiovascular risk, residual inflammatory risk and treatment-related limitations highlight the need for complementary anti-inflammatory strategies. Delphinidin (Dp), a naturally occurring anthocyanidin found in several medicinal plants used in traditional Chinese medicine, exhibits anti-inflammatory activity; however, its effects on macrophage inflammatory signaling and their potential relevance to vascular inflammation remain incompletely understood. This study integrated network pharmacology, molecular docking, molecular dynamics simulations, surface plasmon resonance (SPR), and in vitro experiments to elucidate the mechanisms underlying Dp-mediated regulation of macrophage inflammation. Network analyses identified AKT1 as a candidate target and the PI3K/Akt signaling pathway as a potential regulatory mechanism. Molecular docking and molecular dynamics simulations suggested a structurally plausible interaction between Dp and AKT1, and SPR analysis provided experimental evidence of direct binding between Dp and AKT1. In lipopolysaccharide (LPS)-stimulated RAW264.7 macrophages, Dp reduced NO production and the levels of inducible nitric oxide synthase (iNOS), cyclooxygenase-2 (COX-2), interleukin-1β (IL-1β), interleukin-6 (IL-6), and tumor necrosis factor-α (TNF-α). Dp also decreased the phosphorylation of PI3K (p-PI3K), Akt (p-Akt), and NF-κB (p-NF-κB), while pharmacological interventions further supported the involvement of the PI3K/Akt/NF-κB signaling pathway. Collectively, these findings suggest that Dp attenuates macrophage inflammatory responses, at least in part, by modulating this signaling pathway. These findings provide a basis for further investigation of the anti-inflammatory effects of Dp in macrophages and their potential relevance to vascular inflammation.

Keywords: network pharmacology; molecular docking; molecular dynamics simulation; surface plasmon resonance; delphinidin; vascular inflammation; macrophage inflammation; PI3K/Akt signaling pathway

Check for updates

Academic Editor: Raffaele Capasso

Received: 18 September 2026
Revised: 2 November 2026
Accepted: 17 November 2026
Published: 19 November 2026

Copyright: © 2026 by the authors. Licensee MDPI, Basel, Switzerland. This article is an open access article distributed under the terms and conditions of the Creative Commons Attribution (CC BY) license.

1. Introduction

Macrophage-mediated inflammation is an important component of vascular pathobiology [1]. Activated macrophages respond to metabolic and tissue-derived signals, release inflammatory mediators, and interact with endothelial, vascular smooth muscle, and other immune cells, thereby influencing vascular homeostasis and pathological remodeling [1]. Atherosclerosis (AS) represents one prominent lipid-driven vascular disease in which macrophage inflammatory programs are closely coupled to modified lipoprotein uptake, foam-cell formation, and multicellular interactions within the arterial wall [2,3]. Recent single-cell analyses of human plaques have further revealed heterogeneous macrophage states [4], including inflammatory lipid-associated populations linked to cerebrovascular complications [5]. Despite contemporary lipid-lowering therapy, residual inflammatory risk remains clinically important and is strongly associated with subsequent cardiovascular events and mortality among statin-treated patients [6]. The cardiovascular benefits observed with selected anti-inflammatory interventions further support the clinical relevance of vascular inflammation [7,8]. Accordingly, identifying compounds that modulate macrophage inflammatory signaling may provide mechanistic insights of potential relevance to vascular disease.

Traditional Chinese medicine (TCM) has long been used in the prevention and management of cardiovascular disorders. The capacity of many TCM-derived bioactive constituents to interact with multiple targets and interconnected signaling pathways has prompted increasing interest in their potential application to multifactorial diseases [9–11]. Delphinidin (Dp) is a naturally occurring anthocyanidin and the aglycone of several anthocyanins, widely distributed in deeply pigmented fruits and vegetables [12,13]. Dp and its glycosylated derivatives have also been reported in medicinal plants used in TCM, including *Ephedra* spp., *Glycyrrhiza* spp., *Crocus sativus*, and *Panax notoginseng* [14–16]. Previous studies have documented the anti-inflammatory and anticancer activities of Dp [17]; however, the molecular targets and signaling pathways underlying its regulation of macrophage inflammatory responses remain incompletely characterized.

To address this knowledge gap, the present study integrated network pharmacology, molecular docking, and molecular dynamics simulations to identify candidate targets and signaling pathways potentially involved in Dp-mediated regulation of macrophage inflammation. SPR was used to assess the binding of Dp to AKT1. Selected computational predictions were subsequently evaluated in LPS-stimulated RAW264.7 macrophages using cell viability, Griess, ELISA, and Western blot assays, with particular attention to the PI3K/Akt/NF-κB signaling pathway. By combining in silico predictions, biophysical binding assessment, and cellular evaluation, this study aimed to investigate the molecular mechanisms underlying the anti-inflammatory effects of Dp in macrophages and to provide mechanistic insights of potential relevance to vascular disease.

2. Results

2.1. Identification of Candidate Targets, PPI Network Analysis, and Human–Mouse Ortholog Mapping

The chemical structure of Dp is shown in Figure 1A. Target prediction using SwissTargetPrediction yielded 98 putative Dp-associated targets. In parallel, searches of the GeneCards, OMIM, and TTD databases identified 4661 AS-related targets and 3621 inflammation-related targets. Intersection of the three target sets identified 60 shared candidate targets among the Dp-associated, AS-related, and inflammation-related target sets (Figure 1B and Table 1).

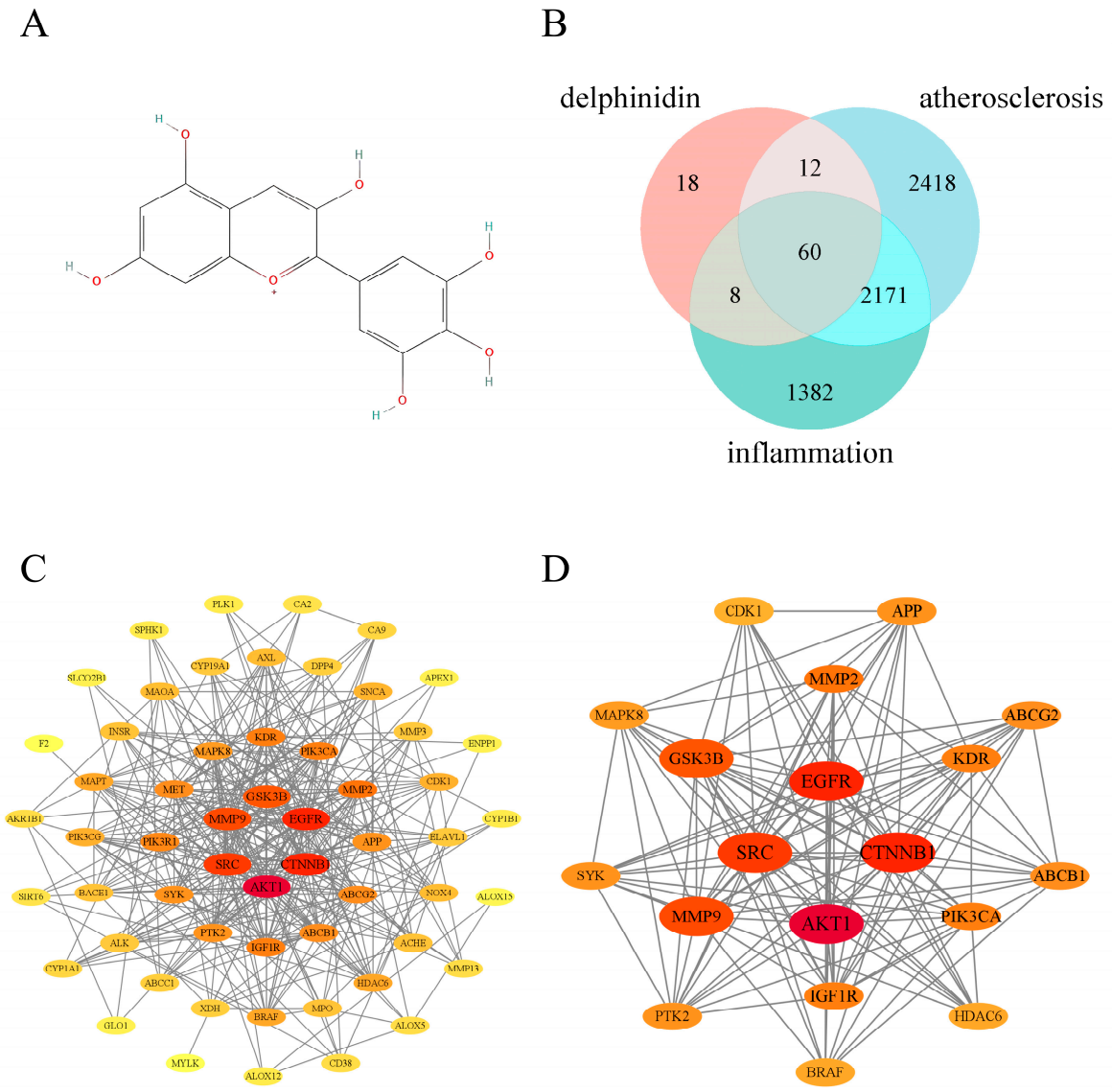


Figure 1. Identification of shared candidate targets of Dp and construction of the protein–protein interaction (PPI) network. (**A**) Chemical structure of Dp. (**B**) Venn diagram showing 60 shared targets among the predicted targets of Dp and AS- and inflammation-related target sets. (**C**) PPI network comprising 57 targets; three disconnected nodes were excluded. (**D**) Nineteen core candidate targets identified using CytoNCA. Node size and color intensity represent degree centrality.

Table 1. Sixty intersecting targets among Dp, AS, and inflammation.

Gene Symbol							
GLO1	*SNCA*	*KDR*	*EGFR*	*NR1H3*	*DPP4*	*F2*	*BACE1*
GSK3B	*PIK3CA*	*MAPT*	*MET*	*MMP2*	*ABCB1*	*APP*	*SIRT6*
APEX1	*ALK*	*PTK2*	*AXL*	*SRC*	*IGF1R*	*CD38*	*HDAC6*
CYP1B1	*MYLK*	*PIK3CG*	*XDH*	*SYK*	*ABCC1*	*ENPP1*	*ACHE*
MAOA	*PNLIP*	*BRAF*	*INSR*	*MMP13*	*MMP9*	*CA9*	*CA2*
ABCG2	*TRPC5*	*SPHK1*	*NOX4*	*ELAVL1*	*PLK1*	*CTNNB1*	*AKT1*
PIK3R1	*ALOX12*	*ALOX15*	*AKR1B1*	*CYP19A1*	*ALOX5*	*MMP3*	*CDK1*
MPO	*CYP1A1*	*SLCO2B1*	*MAPK8*				

The 60 overlapping targets were subsequently subjected to protein–protein interaction (PPI) network analysis. After three disconnected targets were excluded, the resulting

network comprised 57 nodes and 356 edges (Figure 1C). Topological analysis using CytoNCA identified 19 core targets whose values exceeded the corresponding medians for all six predefined centrality parameters (Figure 1D and Table 2). These targets were AKT1, CTNNB1, EGFR, SRC, MMP9, GSK3B, MMP2, PIK3CA, IGF1R, KDR, ABCG2, ABCB1, PTK2, APP, SYK, MAPK8, HDAC6, BRAF, and CDK1. Among these targets, AKT1 exhibited the highest topological importance and was therefore prioritized as a central candidate node for subsequent analyses.

Table 2. Nineteen core candidate targets identified by PPI network analysis and their mouse orthologs.

Number	Gene Symbol	UniProt ID	Gene Full Name	Mouse Ortholog
1	*AKT1*	P31749	AKT serine/threonine kinase 1	*Akt1*
2	*CTNNB1*	P35222	catenin beta 1	*Ctnnb1*
3	*EGFR*	P00533	epidermal growth factor receptor	*Egfr*
4	*SRC*	P12931	SRC proto-oncogene, non-receptor tyrosine kinase	*Src*
5	*MMP9*	P14780	matrix metallopeptidase 9	*Mmp9*
6	*GSK3B*	P49841	glycogen synthase kinase 3 beta	*Gsk3b*
7	*MMP2*	P08253	matrix metallopeptidase 2	*Mmp2*
8	*PIK3CA*	P42336	phosphatidylinositol-4,5-bisphosphate 3-kinase catalytic subunit alpha	*Pik3ca*
9	*IGF1R*	P08069	insulin like growth factor 1 receptor	*Igf1r*
10	*KDR*	P35968	kinase insert domain receptor	*Kdr*
11	*ABCG2*	Q9UNQ0	ATP binding cassette subfamily G member 2 (JR blood group)	*Abcg2*, *Abcg3*
12	*ABCB1*	P08183	ATP binding cassette subfamily B member 1	*Abcb1a*, *Abcb1b*
13	*PTK2*	Q05397	protein tyrosine kinase 2	*Ptk2*
14	*APP*	P05067	amyloid beta precursor protein	*App*
15	*SYK*	P43405	spleen associated tyrosine kinase	*Syk*
16	*MAPK8*	P45983	mitogen-activated protein kinase 8	*Mapk8*
17	*HDAC6*	Q9UBN7	histone deacetylase 6	*Hdac6*
18	*BRAF*	P15056	B-Raf proto-oncogene, serine/threonine kinase	*Braf*
19	*CDK1*	P06493	cyclin dependent kinase 1	*Cdk1*

Human–mouse ortholog mapping identified corresponding mouse orthologs for all 60 shared human candidate target genes. Because some human targets exhibited one-to-many orthologous relationships, a total of 62 mapping records were obtained. Further examination of the 19 core candidate targets identified through PPI network analysis confirmed that *AKT1*, *CTNNB1*, *EGFR*, *SRC*, *MMP9*, *GSK3B*, *MMP2*, *PIK3CA*, *IGF1R*, *KDR*, *ABCG2*, *ABCB1*, *PTK2*, *APP*, *SYK*, *MAPK8*, *HDAC6*, *BRAF*, and *CDK1* all had corresponding mouse orthologs. Among these core targets, *ABCB1* and *ABCG2* each mapped to multiple mouse orthologs, whereas the remaining 17 exhibited one-to-one correspondences in the mapping dataset. These findings support cross-species interpretation of the experimental results obtained in murine RAW264.7 macrophages (Table 2).

2.2. GO Functional and KEGG Pathway Enrichment Analyses

To characterize the potential biological functions of the 60 intersecting targets, GO functional enrichment and KEGG pathway enrichment analyses were performed. At a significance threshold of $p < 0.05$, 221 biological process (BP), 51 cellular component (CC), and 82 molecular function (MF) terms were identified. The 10 most significantly enriched terms in each GO category were selected for visualization. Representative BP terms included negative regulation of apoptotic process, positive regulation of phosphatidylinositol 3-kinase/protein kinase B signal transduction, epidermal growth factor receptor signaling pathway, and insulin receptor signaling pathway (Figure 2A). The CC terms were mainly

associated with the plasma membrane, perinuclear region of cytoplasm, signaling receptor complex, and membrane raft (Figure 2B), whereas the MF terms were predominantly related to protein kinase activity, protein tyrosine kinase activity, ATP binding, and enzyme binding (Figure 2C).

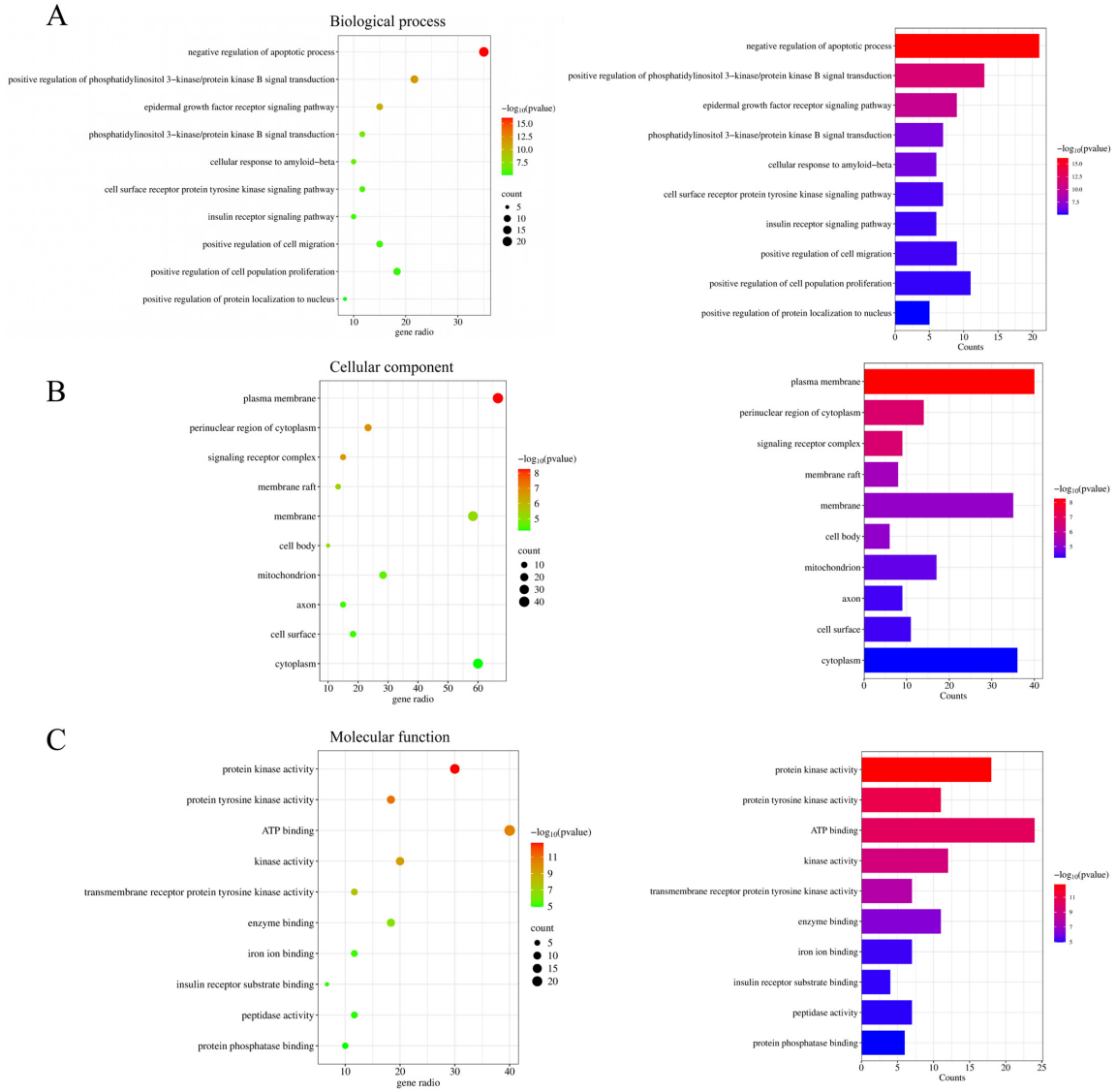


Figure 2. GO enrichment analysis of the 60 intersecting targets. (**A**) Biological process (BP); (**B**) cellular component (CC); and (**C**) molecular function (MF). Bubble plots (**left**) and bar charts (**right**) show the top 10 enriched terms in each category. Bubble position indicates the gene ratio, bubble size and bar length indicate the gene count, and color represents −log10(*p*-value).

KEGG enrichment analysis identified 117 significantly enriched pathways ($p < 0.05$). Among the 30 most significantly enriched pathways were EGFR tyrosine kinase inhibitor resistance, focal adhesion, fluid shear stress and atherosclerosis, FoxO signaling pathway, lipid and atherosclerosis, and PI3K-Akt signaling pathway (Figure 3A and Table 3). Gene–pathway association analysis showed that *AKT1*, *PIK3CA*, and *PIK3R1* were each associated with 29 pathways and exhibited the highest pathway connectivity. In comparison, *EGFR* and *BRAF* were associated with 21 and 19 pathways, respectively (Figure 3B). Collectively, the PPI network and enrichment results supported the prioritization of AKT1 and the PI3K-Akt signaling pathway for further investigation of Dp-mediated regulation of macrophage inflammation, with potential relevance to vascular disease. All 19 core tar-

gets were subsequently subjected to molecular docking, and the Dp–AKT1 complex was selected for molecular dynamics simulation based on the integrated network, enrichment, and docking results.

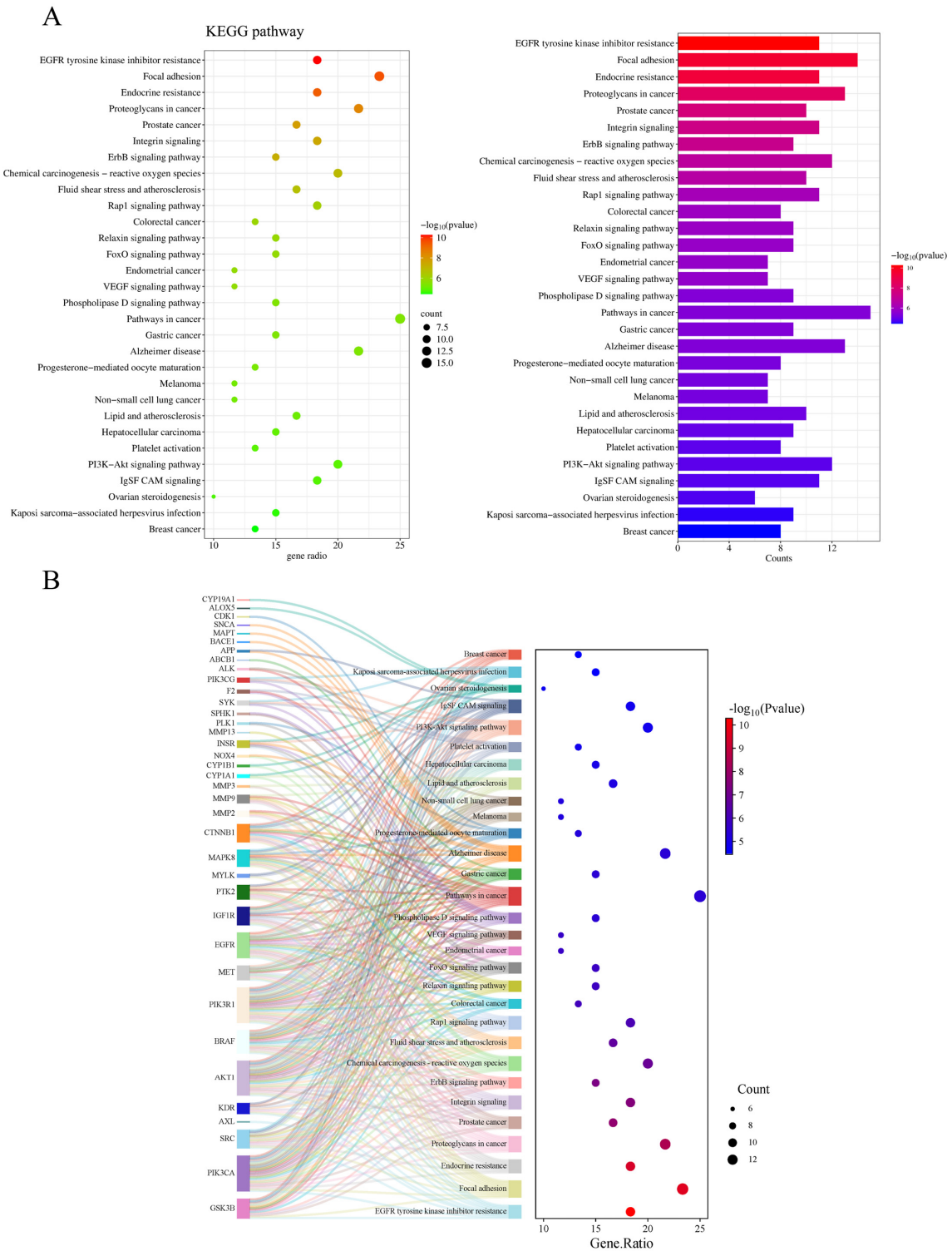


Figure 3. KEGG pathway enrichment analysis of the 60 intersecting targets. (**A**) Bubble plot (left) and bar chart (right) of the top 30 enriched KEGG pathways. (**B**) Sankey diagram showing target–pathway associations. Bubble position indicates the gene ratio, bubble size and bar length indicate the gene count, and color represents −log10(*p*-value).

Table 3. Top 30 enriched KEGG pathways and associated target genes.

No.	Pathway	Target Genes	Count
1	Pathways in cancer	*ALK, GSK3B, MMP2, BRAF, PIK3R1, F2, MMP9, EGFR, PTK2, IGF1R, MAPK8, PIK3CA, AKT1, CTNNB1, MET*	15
2	Focal adhesion	*GSK3B, SRC, BRAF, PIK3R1, EGFR, PTK2, IGF1R, MYLK, MAPK8, PIK3CA, KDR, AKT1, CTNNB1, MET*	14
3	Proteoglycans in cancer	*SRC, MMP2, BRAF, PIK3R1, MMP9, EGFR, PTK2, IGF1R, PIK3CA, KDR, AKT1, CTNNB1, MET*	13
4	Alzheimer disease	*GSK3B, APP, INSR, BRAF, PIK3R1, BACE1, MAPK8, PIK3CA, NOX4, AKT1, CTNNB1, MAPT, SNCA*	13
5	Chemical carcinogenesis–reactive oxygen species	*MAPK8, PIK3CA, SRC, CYP1A1, CYP1B1, NOX4, AKT1, BRAF, PIK3R1, MET, PTK2, EGFR*	12
6	PI3K-Akt signaling pathway	*GSK3B, SYK, PIK3CA, INSR, KDR, AKT1, PIK3R1, MET, PTK2, EGFR, PIK3CG, IGF1R*	12
7	EGFR tyrosine kinase inhibitor resistance	*GSK3B, PIK3CA, SRC, AXL, KDR, AKT1, BRAF, PIK3R1, MET, EGFR, IGF1R*	11
8	Endocrine resistance	*MAPK8, PIK3CA, SRC, MMP2, AKT1, BRAF, PIK3R1, MMP9, PTK2, EGFR, IGF1R*	11
9	Integrin signaling	*GSK3B, PIK3CA, SRC, KDR, CTNNB1, AKT1, PIK3R1, MET, PTK2, EGFR, IGF1R*	11
10	Rap1 signaling pathway	*PIK3CA, SRC, INSR, KDR, CTNNB1, AKT1, BRAF, PIK3R1, MET, EGFR, IGF1R*	11
11	IgSF CAM signaling	*GSK3B, APP, MAPK8, PIK3CA, SRC, KDR, CTNNB1, AKT1, PIK3R1, PTK2, MYLK*	11
12	Prostate cancer	*GSK3B, PIK3CA, MMP3, CTNNB1, AKT1, BRAF, PIK3R1, MMP9, EGFR, IGF1R*	10
13	Fluid shear stress and atherosclerosis	*MAPK8, PIK3CA, SRC, MMP2, KDR, CTNNB1, AKT1, PIK3R1, MMP9, PTK2*	10
14	Lipid and atherosclerosis	*GSK3B, MAPK8, PIK3CA, SRC, MMP3, CYP1A1, AKT1, PIK3R1, MMP9, PTK2*	10
15	ErbB signaling pathway	*GSK3B, MAPK8, PIK3CA, SRC, AKT1, BRAF, PIK3R1, PTK2, EGFR*	9
16	Relaxin signaling pathway	*MAPK8, MMP13, PIK3CA, SRC, MMP2, AKT1, PIK3R1, MMP9, EGFR*	9
17	FoxO signaling pathway	*MAPK8, PIK3CA, INSR, PLK1, AKT1, BRAF, PIK3R1, EGFR, IGF1R*	9
18	Phospholipase D signaling pathway	*SYK, PIK3CA, INSR, SPHK1, AKT1, PIK3R1, F2, EGFR, PIK3CG*	9
19	Gastric cancer	*GSK3B, ABCB1, PIK3CA, CTNNB1, AKT1, BRAF, PIK3R1, MET, EGFR*	9
20	Hepatocellular carcinoma	*GSK3B, PIK3CA, CTNNB1, AKT1, BRAF, PIK3R1, MET, EGFR, IGF1R*	9
21	Kaposi sarcoma-associated herpesvirus infection	*GSK3B, MAPK8, SYK, PIK3CA, SRC, CTNNB1, AKT1, PIK3R1, PIK3CG*	9

Table 3. *Cont.*

No.	Pathway	Target Genes	Count
22	Colorectal cancer	*GSK3B, MAPK8, PIK3CA, CTNNB1, AKT1, BRAF, PIK3R1, EGFR*	8
23	Progesterone-mediated oocyte maturation	*MAPK8, PIK3CA, PLK1, CDK1, AKT1, BRAF, PIK3R1, IGF1R*	8
24	Platelet activation	*SYK, PIK3CA, SRC, AKT1, PIK3R1, F2, PIK3CG, MYLK*	8
25	Breast cancer	*GSK3B, PIK3CA, CTNNB1, AKT1, BRAF, PIK3R1, EGFR, IGF1R*	8
26	Endometrial cancer	*GSK3B, PIK3CA, CTNNB1, AKT1, BRAF, PIK3R1, EGFR*	7
27	VEGF signaling pathway	*PIK3CA, SRC, SPHK1, KDR, AKT1, PIK3R1, PTK2*	7
28	Melanoma	*PIK3CA, AKT1, BRAF, PIK3R1, MET, EGFR, IGF1R*	7
29	Non-small cell lung cancer	*ALK, PIK3CA, AKT1, BRAF, PIK3R1, MET, EGFR*	7
30	Ovarian steroidogenesis	*ALOX5, INSR, CYP1A1, CYP1B1, CYP19A1, IGF1R*	6

2.3. Molecular Docking Analysis

Molecular docking was performed to evaluate the potential interactions between Dp and the 19 core candidate target proteins identified by PPI network analysis, including AKT1, ABCB1, ABCG2, APP, BRAF, CDK1, CTNNB1, EGFR, GSK3B, HDAC6, IGF1R, KDR, MAPK8, MMP2, MMP9, PIK3CA, PTK2, SRC, and SYK. The predicted binding energies of the 19 Dp–protein complexes ranged from −10.3 to −5.6 kcal/mol (Table 4). Among these proteins, MMP9 yielded the most favorable docking score (−10.3 kcal/mol), followed by KDR (−9.0 kcal/mol), EGFR (−8.4 kcal/mol), and ABCB1, HDAC6, and SYK (−8.3 kcal/mol each). The predicted binding energies of the remaining complexes ranged from −8.2 to −5.6 kcal/mol. Within the same docking protocol, these negative scores indicated energetically favorable predicted interactions between Dp and the tested proteins, with more negative values representing more favorable docking predictions.

Table 4. Molecular docking interactions and binding energies of Dp with the 19 core target proteins.

Target Protein	Component	Bond Type	Interaction Position	Binding Energy (kcal/mol)
ABCB1	delphinidin	Hydrophobic interaction	ALA987, VAL991	−8.3
		Hydrogen bond	ASN721	
		Pi-Pi T-shaped	TRP232, PHE303	
		Pi-Sigma	–	
		Carbon–Hydrogen Bond	–	
		Conventional Hydrogen Bond	LEU724, GLN725, GLY722, ASN842, GLN990, MET876, ILE299, PHE994, LEU236, PHE770, GLN838	
ABCG2	delphinidin	Hydrophobic interaction	LEU447	−7.3
		Hydrogen bond	ASN387, GLN398	
		Pi-Pi T-shaped	–	
		Pi-Sigma	–	

Table 4. *Cont.*

Target Protein	Component	Bond Type	Interaction Position	Binding Energy (kcal/mol)
		Carbon–Hydrogen Bond	LEU478	
		Conventional Hydrogen Bond	LEU388, ASN391, VAL450, SER443, GLU446, ASP477, ALA444, MET481	
AKT1	delphinidin	Hydrophobic interaction	–	−5.8
		Hydrogen bond	GLU17, ARG86, ASN54, GLN79	
		Pi-Pi T-shaped	–	
		Pi-Sigma	–	
		Carbon–Hydrogen Bond	GLY16, ASN53	
		Conventional Hydrogen Bond	TYR18, LYS14, PHE55, ARG25, LEU52	
APP	delphinidin	Hydrophobic interaction	–	−5.6
		Hydrogen bond	ASP167	
		Pi-Pi T-shaped	–	
		Pi-Sigma	–	
		Carbon–Hydrogen Bond	–	
		Conventional Hydrogen Bond	CYS133, VAL185, GLY169, TYR168, GLU183, PHE184	
BRAF	delphinidin	Hydrophobic interaction	ALA23, VAL51	−6.3
		Hydrogen bond	TYR48	
		Pi-Pi T-shaped	–	
		Pi-Sigma	VAL95	
		Carbon–Hydrogen Bond	–	
		Conventional Hydrogen Bond	THR90, GLU91, GLY94, THR98, LYS27, ALA24, GLU20	
CDK1	delphinidin	Hydrophobic interaction	VAL64, ALA145	−7.7
		Hydrogen bond	TYR15, GLN132, ASP146	
		Pi-Pi T-shaped	–	
		Pi-Sigma	LEU135	
		Carbon–Hydrogen Bond	–	
		Conventional Hydrogen Bond	GLU12, GLY11, VAL18, ILE10, ALA31, PHE80, LEU55, LYS33	
CTNNB1	delphinidin	Hydrophobic interaction	–	−7.4
		Hydrogen bond	ARG181, ASP183	
		Pi-Pi T-shaped	–	
		Pi-Sigma	THR31	
		Carbon–Hydrogen Bond	GLY239	
		Conventional Hydrogen Bond	THR240, GLN32, TYR27, ASP30, ARG48, PRO50, THR178, LEU179	
EGFR	delphinidin	Hydrophobic interaction	ALA743, VAL726	−8.4
		Hydrogen bond	GLN791, MET793	
		Pi-Pi T-shaped	–	

Table 4. *Cont.*

Target Protein	Component	Bond Type	Interaction Position	Binding Energy (kcal/mol)
		Pi-Sigma	LEU844	
		Carbon–Hydrogen Bond	–	
		Conventional Hydrogen Bond	MET790, LEU792, LEU718, GLY796, CYS797, GLY719, SER720, PHE723, ASN842, ARG841, PHE856	
GSK3B	delphinidin	Hydrophobic interaction	ALA179, ALA232, MET282, VAL166, MET229, LEU158	−8.2
		Hydrogen bond	GLU230, GLU279	
		Pi-Pi T-shaped	–	
		Pi-Sigma	MET282, VAL166	
		Carbon–Hydrogen Bond	–	
		Conventional Hydrogen Bond	THR213, TYR231, PHE439, GLY159, ASN280, LYS277, GLY161, LYS160, THR292, LYS165	
HDAC6	delphinidin	Hydrophobic interaction	ARG1155	−8.3
		Hydrogen bond	ASP1178, TRP1143, TYR1184	
		Pi-Pi T-shaped	–	
		Pi-Sigma	–	
		Carbon–Hydrogen Bond	–	
		Conventional Hydrogen Bond	TYR1156, GLU1141, ILE1177, SER1175, GLY1154, LEU1162, MET1161, TRP1182	
IGF1R	delphinidin	Hydrophobic interaction	LEU1096	−7.5
		Hydrogen bond	ASP1123, TYR950, ASN1110, THR1127	
		Pi-Pi T-shaped	HIS1103	
		Pi-Sigma	–	
		Carbon–Hydrogen Bond	–	
		Conventional Hydrogen Bond	MET1126, GLY1122, PHE1124, GLU949, GLU1020, PHE1027, VAL1023, SER952, PHE1101, VAL1102	
KDR	delphinidin	Hydrophobic interaction	VAL916, ALA866, LEU840	−9
		Hydrogen bond	LYS868	
		Pi-Pi T-shaped	–	
		Pi-Sigma	LEU840, LEU1035, VAL848	
		Carbon–Hydrogen Bond	–	
		Conventional Hydrogen Bond	GLY922, PHE918, VAL899, PHE1047, ASP1046, GLU885, VAL914, VAL867	
MAPK8	delphinidin	Hydrophobic interaction	VAL40, VAL158	−7.9
		Hydrogen bond	SER34, SER155	
		Pi-Pi T-shaped	–	
		Pi-Sigma	ILE32	

Table 4. *Cont.*

Target Protein	Component	Bond Type	Interaction Position	Binding Energy (kcal/mol)
		Carbon–Hydrogen Bond	–	
		Conventional Hydrogen Bond	MET111, LEU110, ALA53, LEU168, ASN156, ALA36, GLN37, LYS55, GLY35, GLY38, GLY33, ALA113	
MMP2	delphinidin	Hydrophobic interaction	PROA29, PROB29	−7.2
		Hydrogen bond	ILE20, ARG19, ARG53	
		Pi-Pi T-shaped	TYR23	
		Pi-Sigma	–	
		Carbon–Hydrogen Bond	TYR23	
		Conventional Hydrogen Bond	ILE21, ILE54, TYR55, ASP33, TYR55, ARG53, GLU30, ASP33, TYRA23	
MMP9	delphinidin	Hydrophobic interaction	LEU188, VAL223, LEU243	−10.3
		Hydrogen bond	ARG249	
		Pi-Pi T-shaped	–	
		Pi-Sigma	–	
		Carbon–Hydrogen Bond	–	
		Conventional Hydrogen Bond	THR251, PRO255, LEU222, TYR248, GLN227, ALA189, HIS236, PRO246, MET247, TYR245, PRO240	
PIK3CA	delphinidin	Hydrophobic interaction	LYS264	−7.6
		Hydrogen bond	LEU262, GLN247	
		Pi-Pi T-shaped	–	
		Pi-Sigma	LYS264	
		Carbon–Hydrogen Bond	–	
		Conventional Hydrogen Bond	PRO217, VAL216, LEU262, GLU263, PRO217, PHE261, LEU252, ILE251, ILE221, TYR250, GLY248	
PTK2	delphinidin	Hydrophobic interaction	ALA452, ILE428	−7.7
		Hydrogen bond	ILE428	
		Pi-Pi T-shaped	–	
		Pi-Sigma	LEU553, ILE428	
		Carbon–Hydrogen Bond	GLY505	
		Conventional Hydrogen Bond	VAL484, GLU500, LEU501, GLU506, SER509, ARG426, GLY429, VAL436, LYS454	
SRC	delphinidin	Hydrophobic interaction	–	−6
		Hydrogen bond	GLU6	
		Pi-Pi T-shaped	–	
		Pi-Sigma	–	
		Carbon–Hydrogen Bond	–	
		Conventional Hydrogen Bond	ALA4, GLU5, THR106, ILE12, TYR8, GLY10, GLN3	

Table 4. *Cont.*

Target Protein	Component	Bond Type	Interaction Position	Binding Energy (kcal/mol)
SYK	delphinidin	Hydrophobic interaction	ALA400, MET448, PRO455, LEU501,	−8.3
		Hydrogen bond	LEU446, LYS402, GLU420	
		Pi-Pi T-shaped	–	
		Pi-Sigma	LEU501, LEU377	
		Carbon–Hydrogen Bond	–	
		Conventional Hydrogen Bond	VAL433, VAL401, LEU417, MER424, PHE513, ASP512, SER511, VAL385, VAL447, GLY454, MET450, GLU452, ALA451	

Analysis of the top-ranked docking poses showed that Dp formed hydrogen-bonding and hydrophobic contacts with residues in the predicted binding pockets of multiple target proteins. Additional aromatic interactions, including π–π T-shaped, π–π stacked, and π–sigma contacts, were predicted in several complexes. These noncovalent contacts may contribute to the orientation and stabilization of Dp within the corresponding predicted binding pockets.

The predicted binding energy of the Dp–AKT1 complex was −5.8 kcal/mol. Although this value was less favorable than those obtained for several other target proteins, AKT1 was prioritized because it occupied a prominent position in the PPI network and was closely associated with the PI3K-Akt signaling pathway identified by enrichment analysis. In the top-ranked docking pose, Dp was predicted to occupy a binding pocket of AKT1 and to form hydrogen bonds with GLU17, ARG86, ASN54, and GLN79. Additional noncovalent contacts involved TYR18, LYS14, PHE55, ARG25, and LEU52, whereas GLY16 and ASN53 participated in carbon–hydrogen bond interactions (Figure 4). Together, these predicted interactions supported the selection of the Dp–AKT1 complex for subsequent molecular dynamics simulation. More broadly, the docking results suggested a potential multi-target interaction profile for Dp; however, binding to candidate proteins other than AKT1 remains to be examined experimentally.

2.4. Molecular Dynamics Simulation

To evaluate the dynamic stability of the Dp–AKT1 complex, a 100 ns all-atom molecular dynamics (MD) simulation was performed. The resulting trajectory was analyzed using the root-mean-square deviation (RMSD), radius of gyration (Rg), solvent-accessible surface area (SASA), root-mean-square fluctuation (RMSF), and a principal component analysis (PCA)-based free-energy landscape (FEL).

As shown in Figure 5A, the RMSD of the Dp–AKT1 complex increased during the initial stage of the simulation and reached a relatively stable plateau after approximately 30 ns. Thereafter, the RMSD generally fluctuated around 0.28 nm, with only moderate variations during the remainder of the simulation, indicating that the complex maintained overall conformational stability. The Rg values remained within a relatively narrow range centered at approximately 1.40 nm throughout the simulation, although modest fluctuations were observed during the later stages (Figure 5B). These results indicated that no marked expansion or collapse of the simulated structure occurred. Similarly, the SASA fluctuated mainly between approximately 7500 and 8500 $Å^2$ without a sustained increasing or decreasing trend (Figure 5C), suggesting that the overall solvent exposure of the complex remained relatively stable.

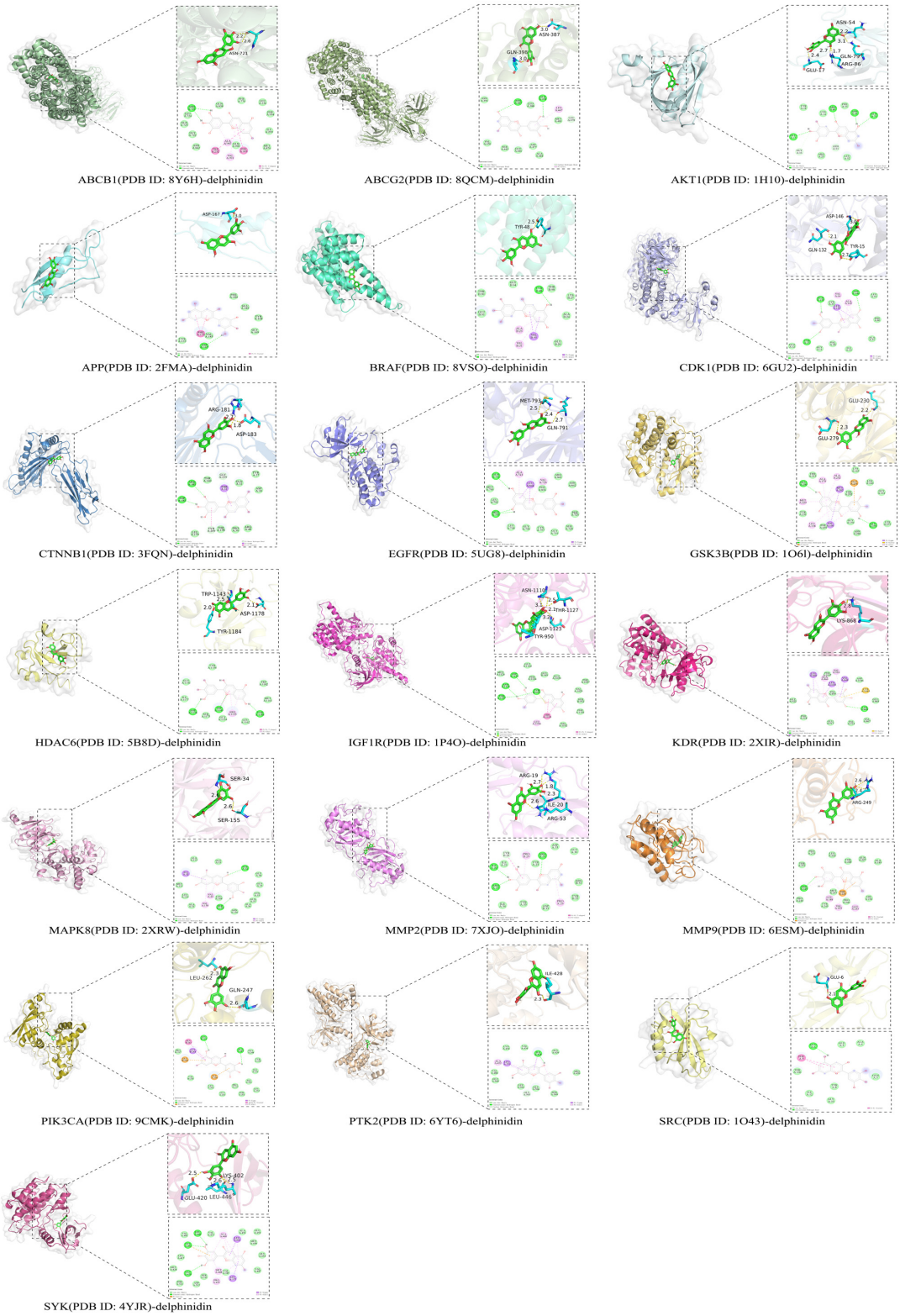


Figure 4. Molecular docking models of Dp with the 19 core target proteins. Three-dimensional binding poses and two-dimensional interaction diagrams show the key interacting residues and interaction types. Dp is shown as green sticks, and hydrogen bonds are indicated by yellow dashed lines.

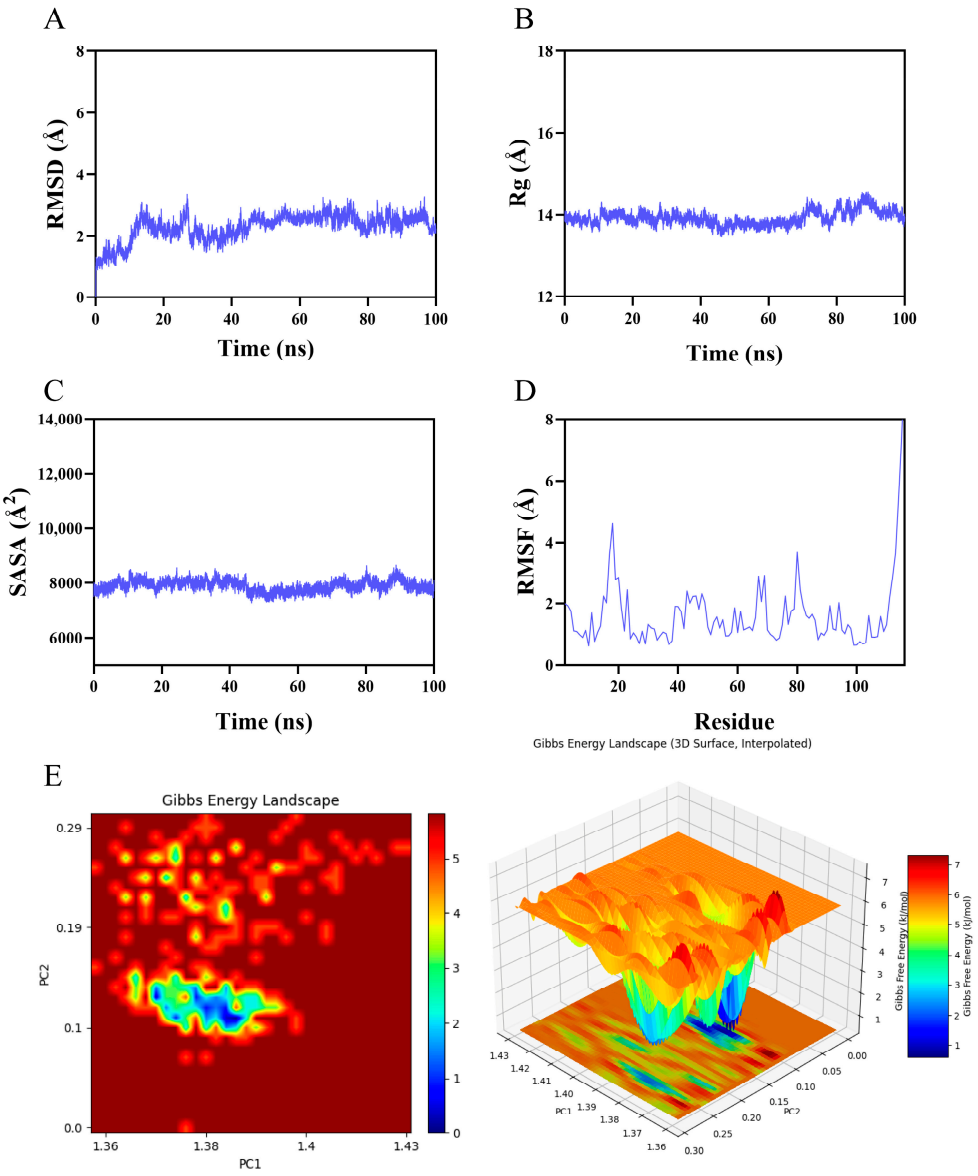


Figure 5. Molecular dynamics analysis of the Dp–AKT1 complex during the 100 ns simulation. (**A**) RMSD; (**B**) Rg; (**C**) SASA; (**D**) RMSF; and (**E**) two- and three-dimensional free-energy landscapes projected onto PC1 and PC2.

Residue-level flexibility was further evaluated using RMSF analysis. As shown in Figure 5D, most residues exhibited RMSF values below approximately 2.5 Å, whereas greater fluctuations were confined to several localized regions and the terminal residues. This pattern indicates that most of the simulated AKT1 structure maintained relatively limited conformational flexibility during the simulation. Furthermore, the FEL projected onto the first two principal components, PC1 and PC2, revealed a predominant low-free-energy basin accompanied by several smaller local minima (Figure 5E). The preferential sampling of this confined low-energy region suggests that the Dp–AKT1 complex predominantly occupied a relatively stable conformational ensemble while retaining limited local flexibility.

Collectively, the RMSD, Rg, SASA, RMSF, and PCA-based FEL analyses were consistent with relatively stable overall conformational behavior of the modeled Dp–AKT1 system within the sampled 100 ns trajectory. These findings complement the molecular docking results and provide computational context for experimental assessment of Dp–AKT1 binding using SPR.

2.5. SPR Analysis of Dp–AKT1 Binding

SPR analysis was performed to examine the interaction between Dp and AKT1 experimentally. AKT1 was immobilized on a CM5 sensor chip, as shown by the immobilization sensorgram (Figure 6A). Dp at concentrations of 3.125–100 μM produced concentration-dependent responses, with signals increasing during analyte injection and decreasing during the subsequent dissociation phase (Figure 6B). Global fitting of the sensorgrams to a 1:1 Langmuir binding model yielded an association rate constant (*ka*) of 2.21 × 10^3 $M^{-1}{\cdot}s^{-1}$ and a dissociation rate constant (*kd*) of 3.82 × 10^{-2} s^{-1}. The corresponding apparent equilibrium dissociation constant (*KD*) was 1.73 × 10^{-5} M (17.3 μM) (Table 5). These findings support an interaction between Dp and immobilized AKT1 under the assay conditions, with an apparent binding affinity in the micromolar range.

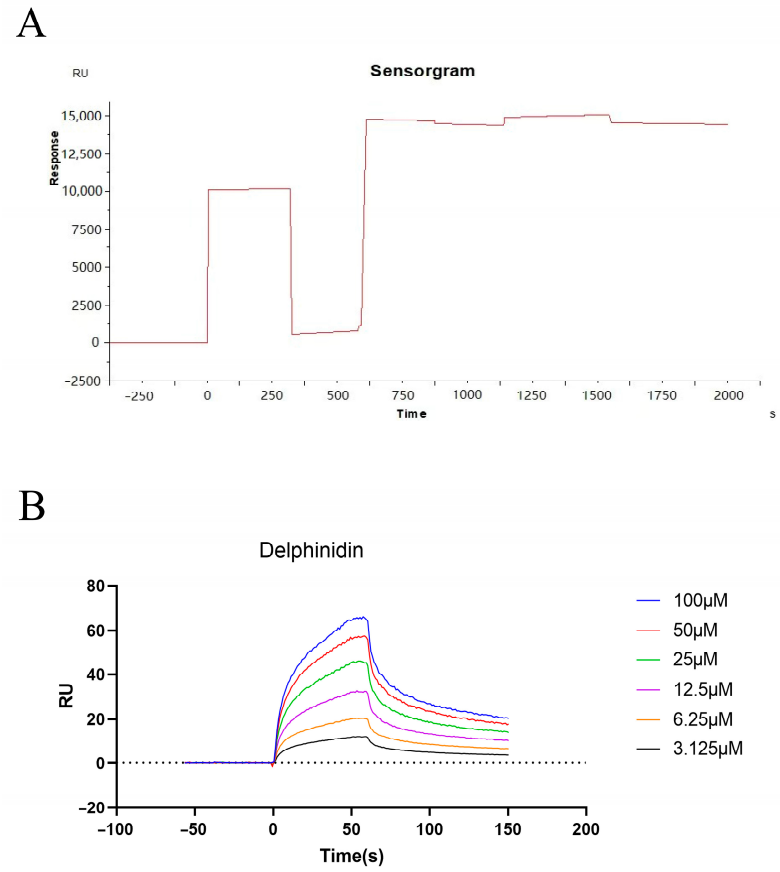


Figure 6. SPR analysis of Dp–AKT1 binding. (**A**) Sensorgram recorded during AKT1 immobilization on a CM5 sensor chip by amine coupling. (**B**) SPR sensorgrams showing the association and dissociation responses of Dp at concentrations of 3.125, 6.25, 12.5, 25, 50, and 100 μM over immobilized AKT1. Different colors correspond to the concentrations indicated in the legend. RU, response units.

Table 5. SPR kinetic parameters for the binding of Dp to AKT1.

Ligand (Immobilized)	Analyte (Flowing)	*ka* ($M^{-1}{\cdot}s^{-1}$)	*kd* (s^{-1})	*KD* (M)
AKT1	Delphinidin	2.21 × 10^{+03}	3.82 × 10^{-02}	1.73 × 10^{-05}

2.6. Dp Attenuates LPS-Induced Inflammatory Responses and NF-κB Activation in RAW264.7 Cells

The effects of Dp on RAW264.7 cell viability were first evaluated using the CCK-8 assay. Dp at concentrations ranging from 20 to 160 μM did not significantly affect cell viability com-

pared with the untreated control group ($p > 0.05$), whereas 320 μM Dp markedly reduced cell viability (Figure 7A). The effect of non-cytotoxic concentrations of Dp on LPS-induced NO production was subsequently examined. LPS stimulation significantly increased NO production compared with the untreated control group. Treatment with 20 μM Dp did not significantly reduce NO production relative to the LPS-treated model group, whereas 40, 80, and 160 μM Dp significantly decreased NO production in a concentration-dependent manner (Figure 7B). Based on the combined results of the CCK-8 and NO assays, 40, 80, and 160 μM Dp were selected for the subsequent experiments.

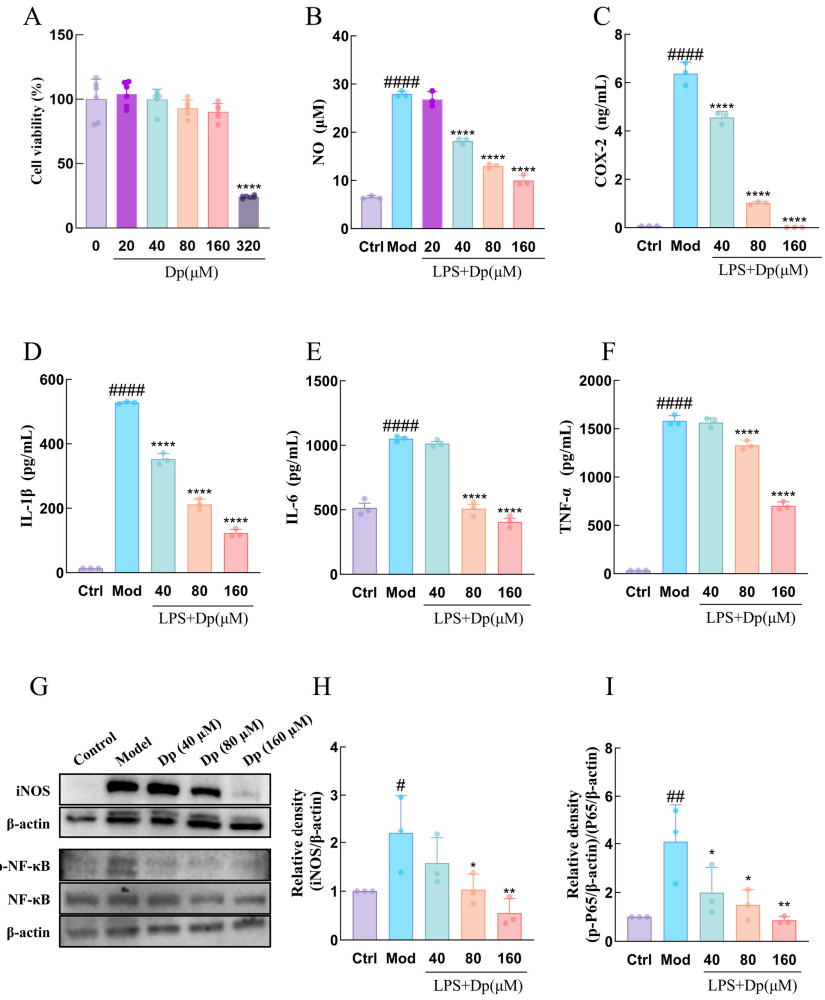


Figure 7. Dp suppresses LPS-induced inflammatory responses in RAW264.7 cells. (**A**) Cell viability assessed by the CCK-8 assay ($n = 6$). (**B**) NO production measured by the Griess assay ($n = 3$). (**C**–**F**) COX-2, IL-1β, IL-6, and TNF-α levels in culture supernatants measured by ELISA ($n = 3$). (**G**) Representative Western blots of iNOS, p-NF-κB p65, NF-κB p65, and β-actin. (**H**,**I**) Quantification of iNOS/β-actin and p-NF-κB p65/NF-κB p65, respectively ($n = 3$). Quantitative data are presented as the mean ± SD from six independent experiments in (**A**) and three independent experiments in (**B**–**F**,**H**,**I**). For the CCK-8 assay, six technical replicates were averaged within each independent experiment, whereas for the Griess and ELISA assays, three technical replicates were averaged before statistical analysis. **** $p < 0.0001$ versus the untreated control group in (**A**); # $p < 0.05$, ## $p < 0.01$, and #### $p < 0.0001$ versus the control group; * $p < 0.05$, ** $p < 0.01$, and **** $p < 0.0001$ versus the LPS-treated model group. Ctrl, untreated control; Mod, LPS-treated model.

ELISA results showed that LPS stimulation markedly increased the levels of COX-2, IL-1β, IL-6, and TNF-α in the cell culture supernatant compared with the untreated control group (Figure 7C–F). Dp treatment significantly reduced the supernatant levels of COX-2

and IL-1β at all three concentrations examined (Figure 7C,D). In contrast, significant reductions in IL-6 and TNF-α levels were observed following treatment with 80 and 160 μM Dp, whereas the reductions observed at 40 μM did not reach statistical significance (Figure 7E,F). Overall, these inflammatory mediators exhibited a concentration-related decreasing trend following Dp treatment.

Consistent with the reduction in NO production, Western blot analysis showed that LPS stimulation significantly increased iNOS protein expression (Figure 7G,H). Treatment with 80 and 160 μM Dp significantly reduced iNOS expression, whereas the reduction observed at 40 μM was not statistically significant. Total NF-κB protein levels did not differ significantly among the groups. However, LPS stimulation significantly increased the p-NF-κB/NF-κB ratio, while treatment with 40, 80, and 160 μM Dp significantly reduced this ratio in a concentration-dependent manner (Figure 7G,I). Collectively, these findings indicate that Dp attenuates LPS-induced inflammatory responses in RAW264.7 cells and that this effect is associated with reduced NF-κB phosphorylation.

2.7. Dp Suppresses the PI3K/Akt/NF-κB Signaling Pathway in LPS-Stimulated RAW264.7 Cells

Given that Dp attenuated LPS-induced inflammatory responses and reduced NF-κB phosphorylation, and that the PI3K/Akt signaling pathway was identified by network pharmacology, the effects of Dp on PI3K/Akt signaling were subsequently examined. LPS stimulation significantly increased the p-PI3K/PI3K and p-Akt/Akt ratios compared with the untreated control group. Dp treatment significantly reduced both ratios in a concentration-related manner, without significantly affecting the total protein levels of PI3K or Akt (Figure 8A–C).

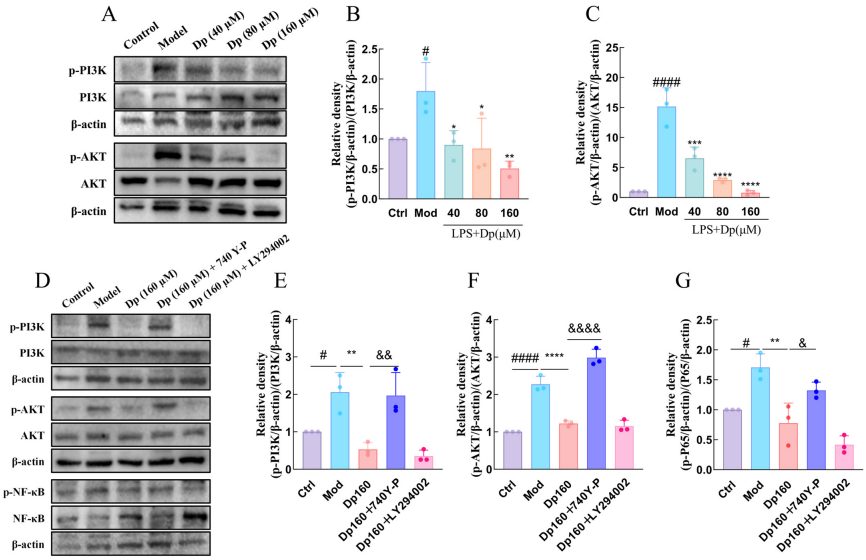


Figure 8. Dp inhibits activation of the PI3K/Akt/NF-κB signaling pathway in RAW264.7 cells. (**A**–**C**) Representative Western blots and quantification of the p-PI3K/PI3K and p-Akt/Akt ratios following treatment with Dp (40, 80, or 160 μM). (**D**–**G**) Representative Western blots and quantification of p-PI3K/PI3K, p-Akt/Akt, and p-NF-κB/NF-κB following treatment with Dp (160 μM) alone or combined with the PI3K activator 740Y-P (5 μM) or inhibitor LY294002 (20 μM). Data are presented as the mean ± SD from three independent experiments ($n = 3$). # $p < 0.05$ and #### $p < 0.0001$ versus the control group; * $p < 0.05$, ** $p < 0.01$, *** $p < 0.001$, and **** $p < 0.0001$ versus the LPS-treated model group; & $p < 0.05$, && $p < 0.01$, and &&&& $p < 0.0001$ versus the Dp (160 μM) group. Ctrl, untreated control; Mod, LPS-treated model.

To further evaluate the involvement of the PI3K/Akt signaling pathway, cells were treated with 160 μM Dp alone or in combination with the PI3K inhibitor LY294002 (20 μM)

or the PI3K activator 740Y-P (5 μM). Compared with Dp treatment alone, co-treatment with LY294002 produced numerical decreases in the p-PI3K/PI3K, p-Akt/Akt, and p-NF-κB/NF-κB ratios, but none of these differences reached statistical significance ($p > 0.05$). In contrast, co-treatment with 740Y-P significantly increased all three phosphorylation ratios relative to Dp treatment alone, partially reversing the Dp-associated reductions in PI3K, Akt, and NF-κB phosphorylation (Figure 8D–G).

Collectively, Dp reduced the phosphorylation of PI3K, Akt, and NF-κB in LPS-stimulated RAW264.7 cells, while 740Y-P partially counteracted these changes. These pharmacological findings further support the involvement of PI3K/Akt signaling in the cellular response to Dp.

3. Discussion

In this study, network pharmacology, molecular docking, molecular dynamics simulations, SPR analysis, and in vitro cellular experiments were combined to investigate the anti-inflammatory effects of Dp in macrophages and the signaling pathways involved, with potential relevance to vascular disease. Network pharmacology prioritized AKT1 as a candidate target and the PI3K/Akt signaling pathway for further investigation. SPR analysis provided direct biophysical evidence of binding between Dp and AKT1. In LPS-stimulated RAW264.7 cells, Dp reduced NO production, iNOS protein expression, and the culture-supernatant levels of COX-2, TNF-α, IL-1β, and IL-6 at non-cytotoxic concentrations. Dp also reduced the p-PI3K/PI3K, p-Akt/Akt, and p-NF-κB/NF-κB ratios without significantly affecting the corresponding total protein levels. Furthermore, co-treatment with LY294002 resulted in additional numerical decreases in these phosphorylation ratios compared with Dp alone, although the differences were not statistically significant, whereas 740Y-P partially reversed the inhibitory effects of Dp. Previous biochemical studies have reported ATP-competitive inhibition of PI3K by Dp [18] and binding of LY294002 within the ATP-binding pocket of PI3K [19]. Taken together, these results support the involvement of PI3K/Akt/NF-κB signaling in the anti-inflammatory response to Dp in LPS-stimulated macrophages.

Network pharmacology identified 60 overlapping targets among the Dp-associated, AS-related, and inflammation-related target sets. Among these targets, AKT1 exhibited high centrality in the protein–protein interaction (PPI) network and was involved in numerous significantly enriched pathways. Other targets, including PIK3CA, PIK3R1, GSK3B, MMP9, EGFR, and SRC, also emerged as prominent components of the PPI network and/or pathway enrichment analysis. Molecular docking suggested possible binding poses between Dp and multiple core candidate proteins, while the 100 ns molecular dynamics simulation indicated that the modeled Dp–AKT1 complex maintained overall conformational stability within the sampled trajectory. Although AKT1 did not produce the most favorable docking score, it was prioritized because of its network centrality and extensive pathway involvement rather than the docking score alone. SPR analysis provided direct biophysical evidence of Dp–AKT1 binding, with an apparent equilibrium dissociation constant of 17.3 μM (Figure 6 and Table 5). This finding supports AKT1 as a Dp-binding protein and complements the cellular evidence implicating PI3K/Akt signaling in the response to Dp. Moreover, the comparatively favorable docking scores obtained for proteins such as MMP9 suggest possible interactions with additional candidate targets, although docking scores across different proteins should not be interpreted as direct quantitative comparisons of binding affinity [20]. Therefore, the roles of these additional candidate targets and their potential interactions require further biochemical and cellular validation [21–23].

Consistent with the possibility that Dp acts through multiple targets, the anti-inflammatory effects observed in the present study broadly agree with previous findings.

Hou et al. reported that Dp reduced COX-2 mRNA and protein expression and inhibited IκBα degradation, NF-κB p65 nuclear translocation, and the activation of JNK, ERK, and p38 MAPK in LPS-stimulated RAW264.7 macrophages [24]. Haseeb et al. found that Dp suppressed IL-1β-induced NF-κB activation in human articular chondrocytes by inhibiting IRAK1 phosphorylation at Ser376 [25]. Neves et al. further showed that delphinidin-3-O-glucoside reduced NF-κB expression in mesenchymal stem cells and modified their secretome, thereby attenuating pro-inflammatory macrophage activation [26]. Consistent with these observations, Dp reduced NO production, iNOS expression, COX-2 and pro-inflammatory cytokine levels, and NF-κB phosphorylation in the present study. Pharmacological modulation of PI3K using LY294002 and 740Y-P further supported the involvement of the PI3K/Akt signaling pathway in the anti-inflammatory effects of Dp. Whereas previous studies have predominantly focused on the MAPK, IRAK1, or IκBα/NF-κB signaling pathways [27,28], the present findings additionally implicate PI3K/Akt signaling in the response to Dp. These observations are not necessarily contradictory but may reflect the ability of Dp to modulate multiple interconnected signaling pathways. Differences in the chemical form of Dp, cell type, inflammatory stimulus, treatment concentration, and exposure duration may also contribute to the variation among studies.

Previous studies have reported protective effects of Dp and its glycosides in vascular endothelial injury models, whereas its effects on macrophage inflammation remain less well characterized. Jin et al. reported that delphinidin-3-glucoside attenuated oxidized low-density lipoprotein (oxLDL)-induced mitochondrial dysfunction in human umbilical vein endothelial cells through SGLT1-mediated cellular uptake [29]. Similarly, Martin et al. reported that Dp protected bovine aortic endothelial cells from apoptosis induced by actinomycin D or 7β-hydroxycholesterol, with the protective effect linked to nitric oxide signaling and calcium homeostasis [30]. These endothelial findings provide context for the possible vascular relevance of Dp, but do not establish its effects on macrophages within atherosclerotic plaques. The studies differed from the present experiments in cell type and experimental stimulus, and Jin et al. used a glycosylated derivative rather than the Dp aglycone tested here. Glycosylation may alter compound stability, cellular uptake, and metabolic behavior [4,31,32]. In the present study, LPS-stimulated RAW264.7 cells were used to examine macrophage inflammatory responses and associated signaling. This model permits assessment of inflammatory activation but is not a disease-specific model of AS. NF-κB signaling and pro-inflammatory cytokines also contribute to vascular inflammation [3], but these responses are not specific to AS. The inclusion of AS-related targets in the network analysis guided candidate selection; it does not establish that the effects observed in the cellular experiments are AS-specific. LPS stimulation does not reproduce the chronic lipid-driven plaque environment, including exposure to modified lipoproteins and cholesterol crystals and interactions among vascular and immune cells [3,32]. The present experiments did not include oxLDL stimulation or assess lipid accumulation and foam-cell formation. Accordingly, the results support an anti-inflammatory effect of Dp in LPS-stimulated macrophages, with potential relevance to vascular disease. Whether Dp also attenuates lipid-driven macrophage inflammation in AS remains to be established.

The effects of PI3K/Akt signaling on macrophage inflammation and lipid metabolism depend on the experimental context [33,34]. Fougerat et al. demonstrated that genetic inactivation or pharmacological inhibition of PI3Kγ attenuated atherosclerotic lesion development and promoted plaque stability in mice by modulating inflammatory cell recruitment and activation [35]. However, this isoform-specific finding cannot be directly equated with the phosphorylation changes observed following Dp treatment. Conversely, Wang et al. reported that miR-223 activated PI3K/Akt signaling while suppressing TLR4/NF-κB signaling, lipid accumulation, and pro-inflammatory cytokine production in macrophages [36].

Arranz et al. further found that Akt1 deficiency enhanced pro-inflammatory macrophage responses [37]. Genetic deficiency and Dp treatment are different interventions, and the present experiments did not establish the functional contribution of individual isoforms. In our study, Dp reduced inflammatory mediator production together with PI3K, Akt, and NF-κB phosphorylation in LPS-stimulated RAW264.7 cells. The partial reversal of these phosphorylation changes by 740Y-P provides additional pharmacological support for pathway involvement, whereas LY294002 produced no significant further reduction. The lack of an additional reduction with LY294002 may reflect limited scope for further suppression after Dp treatment, but does not establish a shared molecular target or binding site. Interpretation of these experiments also requires caution because LY294002 is not exclusively selective for PI3K [38], and effects of pharmacological modulators beyond their intended pathway cannot be excluded. Moreover, phosphorylation measurements at a single time point do not resolve the temporal dynamics of pathway responses. Accordingly, the present findings support the involvement of PI3K/Akt signaling in the response to Dp under the experimental conditions used.

From a methodological perspective, a major strength of this study lies in the complementary use of approaches that provide distinct levels of evidence. Computational analyses helped prioritize candidate targets and pathways. SPR provided experimental evidence of Dp–AKT1 binding, while cellular experiments assessed macrophage inflammatory responses and associated signaling changes. The in vitro experiments measured NO production, iNOS expression, and the levels of COX-2 and three pro-inflammatory cytokines in culture supernatants, thereby reducing reliance on any single inflammatory marker. Dp produced an overall concentration-related reduction in these inflammatory indicators at concentrations that did not significantly affect cell viability as assessed by the CCK-8 assay. In addition, the measurement of both total and phosphorylated PI3K, Akt, and NF-κB enabled protein abundance to be distinguished from relative phosphorylation levels. Pharmacological modulation using LY294002 and 740Y-P provided additional support for pathway involvement through changes in these phosphorylation readouts. Human–mouse ortholog mapping identified corresponding mouse genes for the human-derived candidate targets, providing a gene-level basis for interpreting the computational predictions in the murine experimental system. However, conservation of the predicted signaling relationships and responses to Dp was not directly assessed by functional comparisons between human and murine macrophages and cannot be established from ortholog mapping alone.

Despite these methodological strengths, several limitations should be acknowledged. First, the experiments were confined to an immortalized murine RAW264.7 macrophage-like cell line and an LPS-induced acute inflammatory model. The findings were not validated in primary or human-derived macrophages, under lipid-related stimuli such as oxLDL or cholesterol crystals, or in animal models. Second, the Dp concentrations used in the mechanistic experiments ranged from 40 to 160 μM. Previous cell-based studies provide context for the concentrations examined here. Hou et al. reported concentration-dependent suppression of COX-2 mRNA and protein expression by Dp at concentrations of 25–100 μM in LPS-stimulated murine RAW264 macrophages [24]. In other cellular models, Dp was examined at 50 and 100 μM in LPS-stimulated human airway epithelial cells [39], while Hidalgo et al. evaluated delphinidin chloride at 50, 100, and 150 μM in canine neutrophils [40]. Differences in cell type and treatment conditions limit direct comparison with the present experiments. In our RAW264.7 cells, 20–160 μM Dp did not significantly reduce CCK-8-assessed cell viability, whereas 320 μM did. Dp at 20 μM did not significantly reduce LPS-induced NO production, while 40, 80, and 160 μM produced significant reductions compared with the LPS-treated group. These three concentrations were therefore selected for subsequent in vitro mechanistic experiments, rather than to reproduce known plasma

or tissue exposure. Notably, however, human studies of orally administered Dp glycosides have reported nanomolar plasma concentrations [41], while a recent mouse study reported low, rapidly declining plasma Dp levels under its intraperitoneal dosing regimen [42]. These studies do not establish that exposure comparable to 40–160 μM can be achieved or sustained in vivo. Dp degradation under cell-culture conditions has also been documented [43,44]. Neither the stability of Dp in our culture medium nor its extracellular or intracellular concentrations and degradation products were measured. The relationship between nominal dosing and exposure to intact Dp therefore remains uncertain. Compound selectivity at these concentrations was not examined. Dp has been reported to bind to and inhibit PI3K and MAPKK4 in biochemical assays and UVB-related experimental models [18]. These findings provide a basis for considering protein targets other than AKT1 when interpreting its cellular effects. Goszcz et al. also reported oxygen-centred radical generation by Dp at 100 μM in vitro [44], indicating that concentration-dependent redox effects warrant consideration alongside protein-mediated mechanisms. The contributions of these alternative mechanisms were not examined in our RAW264.7 cells, and nonspecific or additional-target effects cannot be excluded. Third, mechanistic evidence for PI3K/Akt involvement was based mainly on protein phosphorylation measurements and pharmacological interventions. Although NO production, iNOS expression, and inflammatory mediator levels were assessed across Dp concentrations, the pharmacological experiments demonstrated modulation of phosphorylation readouts rather than functional rescue of the inflammatory phenotype. Pathway-specific genetic knockdown, knockout, or rescue experiments were not performed. Direct Akt kinase activity measurements and assessments of NF-κB nuclear translocation or transcriptional activity were also not conducted. These limitations preclude firm conclusions regarding pathway necessity and the specific cellular contribution of AKT1.

In light of these limitations, future studies should focus on testing the findings in disease-relevant models, clarifying target contributions, and relating Dp activity to measured exposure. The key findings should be examined in bone marrow-derived macrophages and human monocyte-derived macrophages using oxidized low-density lipoprotein or cholesterol crystals, with assessment of inflammatory responses, lipid uptake and efflux, and foam cell formation. Disease-specific animal models could then be used to evaluate whether these cellular effects are accompanied by changes in vascular inflammation and pathology. At the mechanistic level, cellular target-engagement assays, isoform-specific genetic knockdown or knockout and rescue experiments involving constitutively active Akt could help clarify the contributions of AKT1, upstream PI3K signaling, and other prioritized targets. The effects of pathway perturbation on NO production, iNOS expression, and cytokine release should be assessed alongside phosphorylation, Akt kinase activity, and NF-κB nuclear translocation or transcriptional activity. Dp stability in culture medium and cellular exposure should also be measured, while plasma and tissue pharmacokinetics would help determine whether exposure levels associated with activity can be achieved in vivo. To address its limited stability and bioavailability, future studies should compare the activities and pharmacokinetic properties of Dp aglycone, its glycosides, and major metabolites, and explore encapsulation or vesicle-based delivery where appropriate [45,46]. Collectively, these studies would clarify the relevance of the present macrophage findings to vascular disease.

4. Materials and Methods

4.1. Reagents

The murine macrophage leukemia cell line RAW264.7 was purchased from the National Biomedical Experimental Cell Resource Bank of China (Beijing, China). The following

were used: 10% fetal bovine serum (Lixin Biotech, Guangzhou, China, KY-01000CM); 1% penicillin–streptomycin (Procell, Wuhan, China, PB180120); high-glucose DMEM (Procell, Wuhan, China, PM150210); lipopolysaccharide (LPS, Ambeed, Buffalo Grove, IL, USA, A1228298); delphinidin (Dp, Yuanye, Shanghai, China, B24337); PI3K activator 740Y-P (Yuanye, Shanghai, China, S80211); PI3K inhibitor LY294002 (Ambeed, Buffalo Grove, IL, USA, A133122); Cell Counting Kit-8 (CCK-8, Elabscience, Wuhan, China, E-CK-A362); nitric oxide (NO) assay kit (Beyotime, Shanghai, China, S0021S); ELISA kits for TNF-α (Elabscience, Shanghai, China, E-EL-M3063), IL-6 (Elabscience, Shanghai, China, E-EL-M0064), IL-1β (Elabscience, Shanghai, China, E-EL-M0037), and COX-2 (Elabscience, Shanghai, China, E-EL-M0959); protease inhibitor (Ambeed, Buffalo Grove, IL, USA, A1320914); phosphatase inhibitor (Ambeed, Buffalo Grove, IL, USA, A2679231); RIPA lysis buffer (WSHT, Shanghai, China, EZPS03-2); BCA protein assay kit (Elabscience, Shanghai, China, E-BC-K318-M); glycine (BioFroxx, Einhausen, Germany, 1275KG2P5); SDS (BioFroxx, Einhausen, Germany, 3250GR500); Tris base (BioFroxx, Einhausen, Germany, 1115GR500); Tris–glycine SDS–PAGE gels (WSHT, Shanghai, China, PSG2001-420F); polyvinylidene fluoride membranes (PVDF membranes, MilliporeSigma, Burlington, MA, US, ISEQ00010); universal rapid blocking buffer (WSHT, Shanghai, China, EZWB04-4); ECL detection kit (Biosharp, Hefei, China, BL523B); acidic antibody stripping buffer (WSHT, Shanghai, China, EZWB03-3); basic antibody stripping buffer (WSHT, Shanghai, China, EZWB03-2); antibody dilution buffer (Elabscience, Shanghai, China, E-IR-R121); Tween-20 (Solarbio, Beijing, China, T8220); and sodium chloride (Sinopharm Chemical Reagent Co., Ltd., Shanghai, China, 10019318). The primary antibodies used for Western blotting were anti-iNOS (Abmart, Shanghai, China, T55993, 1:500), anti-PI3K (Proteintech, Wuhan, China, 60225-1-Ig, 1:5000), anti-p-PI3K (Abmart, Shanghai, China, T40116, 1:1000), anti-Akt (Proteintech, Wuhan, China, 10176-2-AP, 1:2000), anti-p-Akt (Abmart, Shanghai, China, T40067, 1:1000), anti-NF-κB (Abmart, Shanghai, China, T55034, 1:5000), anti-p-NF-κB (Abmart, Shanghai, China, TB3675, 1:1000), and anti-β-actin (Proteintech, Wuhan, China, 20536-1-AP, 1:5000). Goat anti-rabbit IgG (H + L) (Elabscience, Shanghai, China, E-AB-1003, 1:5000) and goat anti-mouse IgG (H + L) (Elabscience, Shanghai, China, E-AB-1001, 1:5000) were used as secondary antibodies. For the SPR experiments, AKT1 protein (Topscience, Boston, MA, US, TMPY-04552), CM5 sensor chips (Cytiva, Uppsala, Sweden, BR100530), an amine coupling kit (Cytiva, Uppsala, Sweden, BR100050), sodium acetate buffer (pH 4.0; Cytiva, Uppsala, Sweden, BR100349), 10× PBS-P+ buffer (Cytiva, Uppsala, Sweden, 28995084), and dimethyl sulfoxide (DMSO, Sigma-Aldrich, Burlington, MA, USA, D8418) were used.

4.2. Prediction of Potential Targets of Dp

The isomeric SMILES string of Dp was retrieved from the PubChem database (https://pubchem.ncbi.nlm.nih.gov/, accessed on 9 November 2025) and submitted to the SwissTargetPrediction database (http://www.swisstargetprediction.ch/, accessed on 9 November 2025). Target prediction was performed with the organism restricted to Homo sapiens. Predicted targets with a probability greater than 0 were retained for subsequent analyses.

4.3. Collection of AS- and Inflammation-Related Targets

Genes associated with AS and inflammation were independently retrieved from the GeneCards database (https://www.genecards.org/, accessed on 9 November 2025) using "atherosclerosis" and "inflammation" as the respective search terms. For each query, entries with a Relevance score greater than twice the median score of the corresponding dataset were retained. In parallel, the same search terms were used to retrieve additional disease-associated targets from the Online Mendelian Inheritance in Man database (OMIM; http://www.omim.org/, accessed on 9 November 2025) and the Therapeutic Target Database

(TTD; https://ttd.idrblab.cn/, accessed on 9 November 2025). The retrieved datasets were subsequently merged, and duplicate entries were removed to generate the final sets of AS- and inflammation-related targets for downstream analyses.

4.4. Identification of Shared Candidate Targets of Dp

Overlapping targets among the predicted Dp targets and the AS- and inflammation-related target sets were identified and visualized using a Venn diagram generated with an online bioinformatics platform (http://www.bioinformatics.com.cn/, accessed on 9 November 2025). The shared targets were retained as candidate targets for subsequent PPI network and enrichment analyses.

4.5. Protein–Protein Interaction Network Construction and Topological Analysis

The intersecting targets identified in Section 2.1 were submitted to the STRING database (https://string-db.org/, accessed on 10 November 2025) for protein–protein interaction (PPI) network construction. "Multiple proteins" was selected as the analysis mode, the organism was restricted to Homo sapiens, and the minimum required interaction score was set to 0.4. Disconnected nodes were excluded from the resulting network. The PPI network data were exported in tab-separated values (TSV) format and subsequently imported into Cytoscape (version 3.10.3) for visualization and topological analysis. The CytoNCA plugin was used to calculate six topological parameters: degree centrality (DC), betweenness centrality (BC), closeness centrality (CC), eigenvector centrality (EC), network centrality (NC), and local average connectivity (LAC). Targets with values exceeding the corresponding median for all six parameters were defined as core candidate targets.

4.6. Gene Ontology and KEGG Pathway Enrichment Analyses

All intersecting targets identified in Section 2.1 were submitted to the Database for Annotation, Visualization and Integrated Discovery (DAVID; https://davidbioinformatics.nih.gov/, accessed on 10 November 2025) for Gene Ontology (GO) functional enrichment and Kyoto Encyclopedia of Genes and Genomes (KEGG) pathway enrichment analyses. The species was restricted to Homo sapiens, and terms with $p < 0.05$ were considered significantly enriched. The enriched terms were ranked according to their p values. The top 10 terms in each GO category—biological process, cellular component, and molecular function—and the top 30 KEGG pathways were visualized using an online bioinformatics platform (http://www.bioinformatics.com.cn/, accessed on 10 November 2025).

4.7. Molecular Docking Analysis

Molecular docking was performed to evaluate the potential interactions between Dp and the 19 core candidate targets identified through PPI network analysis. The two-dimensional structure of Dp was retrieved from the PubChem database (https://pubchem.ncbi.nlm.nih.gov/, accessed on 6 January 2026) and imported into Chem3D (version 23.1.1) for three-dimensional structure generation and energy minimization. The optimized ligand structure was subsequently exported in MOL2 format. High-resolution crystal structures of the target proteins were obtained from the RCSB Protein Data Bank (RCSB PDB; https://www.rcsb.org/, accessed on 6 January 2026). Crystallographic water molecules and nonessential heteroatoms, including phosphate ions, were removed using PyMOL (version 2.6), and the processed protein structures were saved in PDB format [47]. Protein and ligand structures were prepared using AutoDockTools (version 1.5.7) by adding hydrogen atoms and assigning partial charges. Rotatable bonds were defined for the ligand, and the prepared structures were converted to PDBQT format. Molecular docking was then performed using AutoDock Vina (version 1.2.5), with the proteins treated as rigid receptors

and Dp treated as a flexible ligand [48,49]. The center and dimensions of each grid box were defined according to the corresponding protein-binding pocket. For each protein–ligand complex, the conformation with the lowest predicted binding energy was selected as the optimal docking pose. Protein–ligand interactions were visualized using Discovery Studio 2019 and PyMOL (version 2.6) to generate two-dimensional interaction diagrams and three-dimensional binding-mode representations.

4.8. Molecular Dynamics Simulations

The top-ranked docking pose of the Dp–AKT1 complex was used as the initial structure for all-atom molecular dynamics (MD) simulations. The ligand parameters were assigned using the General Amber Force Field 2 (GAFF2), and its partial atomic charges were derived using the restrained electrostatic potential (RESP) method. The AKT1 protein was parameterized using the AMBER ff14SB force field. The complex was solvated in a periodic box containing TIP3P water molecules. Counterions were added to neutralize the net charge of the system, followed by the addition of NaCl to a final concentration of 0.15 M to approximate physiological ionic conditions. Energy minimization was performed in two stages: the solvent molecules and ions were first minimized while the protein–ligand complex was restrained, followed by minimization of the entire system. After gradual heating to 310 K, the system was equilibrated under the isothermal–isobaric (NPT) ensemble. A 100 ns production simulation was subsequently performed. The resulting trajectories were analyzed by calculating the root-mean-square deviation (RMSD), root-mean-square fluctuation (RMSF), radius of gyration (Rg), solvent-accessible surface area (SASA), and free-energy landscape (FEL).

4.9. Surface Plasmon Resonance Analysis

The interaction between Dp and AKT1 was examined by SPR using a Biacore 1K instrument (Cytiva). AKT1 protein was immobilized on a CM5 sensor chip by amine coupling. Following activation with EDC/NHS, AKT1 diluted to 50 μg/mL in sodium acetate buffer (pH 4.0) was injected at a flow rate of 10 μL/min. Unreacted sites were subsequently blocked with ethanolamine. A reference surface was prepared using the same activation and blocking procedures without protein immobilization. Binding measurements were performed using 1× PBS-P+ buffer (pH 7.4) containing 5% (v/v) DMSO. Dp was prepared in PBS containing 5% (v/v) DMSO at concentrations of 3.125, 6.25, 12.5, 25, 50, and 100 μM and injected over the sensor surfaces at 30 μL/min for 60 s per concentration. After each measurement cycle, the surface was regenerated with 10 mM glycine-HCl (pH 2.0) for 5 min. Solvent correction was performed using a DMSO calibration series spanning 4.5–5.8% (v/v). Sensorgrams were processed using Biacore Insight software (version 6.0) by subtracting the reference-surface response from the AKT1-surface response. The corrected sensorgrams were globally fitted to a 1:1 Langmuir binding model to determine the association rate constant (ka) and dissociation rate constant (kd). The apparent equilibrium dissociation constant (KD) was calculated as kd/ka.

4.10. Human–Mouse Ortholog Mapping

Because the network pharmacology and PPI analyses were based on human targets, whereas the in vitro experiments were performed in murine RAW264.7 macrophages, human–mouse ortholog mapping was conducted to support cross-species interpretation of the findings. The 60 shared human candidate target genes identified in Section 2.1 were mapped to their corresponding mouse orthologs using the mouse–human orthology report provided by Mouse Genome Informatics (MGI; https://www.informatics.jax.org/, accessed on 5 October 2026). The recorded information included human and mouse gene symbols

and Entrez Gene IDs, human HGNC IDs, mouse MGI IDs, homology class identifiers, and mapping status.

4.11. Cell Culture and Treatment

The murine macrophage cell line RAW264.7 was maintained in high-glucose Dulbecco's modified Eagle medium (DMEM) supplemented with 10% (*v*/*v*) fetal bovine serum and 1% (*v*/*v*) penicillin–streptomycin. Cells were cultured at 37 °C in a humidified atmosphere containing 5% CO_2. To induce an inflammatory response, cells in all experimental groups except the untreated control group were exposed to LPS at a final concentration of 1 μg/mL. The low-, medium-, and high-concentration Dp groups were treated with 40, 80, and 160 μM Dp, respectively, in the presence of LPS.

4.12. Cell Viability Assay

The effect of Dp on RAW264.7 cell viability was evaluated using a Cell Counting Kit-8 (CCK-8) assay. Cells were seeded in 96-well plates at a density of 1×10^4 cells/well, with six technical replicate wells established for each treatment group, and allowed to adhere for 24 h. The culture medium was then replaced with 100 μL of fresh medium containing the indicated concentrations of Dp, and the cells were incubated for an additional 24 h. After treatment, the medium was removed, and 100 μL of CCK-8 working solution, prepared by mixing culture medium with CCK-8 reagent at a ratio of 9:1 (*v*/*v*), was added to each well. Following incubation at 37 °C in the dark for 1.5 h, absorbance at 450 nm was measured using a Spark multimode microplate reader (Tecan, Männedorf, Switzerland). Cell viability was expressed as a percentage of that in the untreated control group. The assay was performed in six independent experiments (n = 6). Within each experiment, the six technical replicate measurements were averaged to obtain one value per treatment group for statistical analysis.

4.13. Measurement of NO Production

NO production in the culture supernatant was assessed using a Griess-based NO assay kit. RAW264.7 cells in the exponential growth phase were harvested and seeded in 24-well plates, with three technical replicate wells established for each treatment group. After the cells reached approximately 80% confluence, the culture medium was replaced with 500 μL of the corresponding treatment medium prepared according to the group assignments described in Section 4.11. Following incubation for 24 h, 50 μL of culture supernatant from each well was transferred to a 96-well plate. The Griess reaction was performed according to the manufacturer's instructions, and absorbance at 540 nm was measured using a Spark multimode microplate reader (Tecan, Männedorf, Switzerland). The nitrite concentration, used as an indicator of NO production, was determined according to the manufacturer's protocol. The experiment was independently repeated three times, with three technical replicate wells per group in each experiment.

4.14. Quantification of Inflammatory Mediators by ELISA

RAW264.7 cells in the exponential growth phase were harvested and seeded in culture plates. After the cells reached approximately 80% confluence, the culture medium was replaced with 1 mL of the corresponding treatment medium per well, as described in Section 4.11. Following incubation for 24 h, the culture supernatants were collected and clarified by centrifugation. The concentrations of TNF-α, IL-6, and IL-1β, as well as the level of COX-2, in the clarified supernatants were quantified using the corresponding ELISA kits according to the manufacturers' instructions. The experiment was independently repeated three times.

4.15. Western Blot

Total protein was extracted from treated RAW264.7 cells using radioimmunoprecipitation assay (RIPA) lysis buffer supplemented with protease and phosphatase inhibitors. Protein concentrations were determined using a bicinchoninic acid (BCA) assay kit. Equal amounts of protein (20 μg per lane) were separated using 1.0-mm-thick, 15-well Tris–glycine sodium dodecyl sulfate–polyacrylamide gel electrophoresis (SDS–PAGE) gels and subsequently transferred onto 0.2 μm polyvinylidene fluoride (PVDF) membranes. The membranes were blocked with a rapid blocking buffer at 37 °C for 15 min and then washed once with Tris-buffered saline containing Tween-20 (TBST; 20 mM Tris base, 137 mM NaCl, and 0.2% Tween-20) for 5 min. The membranes were incubated with the appropriate primary antibodies overnight at 4 °C. After four washes with TBST for 15 min each, the membranes were incubated with the corresponding horseradish peroxidase-conjugated secondary antibodies at 37 °C for 1 h. Following four additional washes with TBST for 15 min each, immunoreactive bands were detected using an enhanced chemiluminescence substrate and imaged with a ChemiDoc XRS+ imaging system (Bio-Rad, Hercules, CA, USA). Band intensities were quantified using ImageJ software (version 1.54r; National Institutes of Health, Bethesda, MD, USA). The levels of non-phosphorylated target proteins were normalized to the corresponding loading control, whereas phosphorylation levels were expressed as the ratios of phosphorylated proteins to their respective total proteins. The experiment was independently repeated three times.

4.16. Statistical Analysis

All statistical analyses and graphical presentations were performed using GraphPad Prism software (version 10.1.2; GraphPad Software, Boston, MA, USA). Quantitative data are presented as the mean ± standard deviation (SD) of six independent experiments for the CCK-8 assay ($n = 6$) and three independent experiments for the Griess, ELISA, and Western blot assays ($n = 3$). When technical replicates were included, their values were averaged to generate a single value for each treatment group within each independent experiment before statistical analysis. Data distributions and homogeneity of variance were assessed before parametric analyses. For datasets satisfying the assumptions of normality and equal variance, differences among multiple groups were evaluated using one-way analysis of variance (ANOVA). When the overall ANOVA indicated a statistically significant difference, Tukey's multiple-comparisons test was performed for post hoc pairwise comparisons. All statistical tests were two-sided, and $p < 0.05$ was considered statistically significant.

5. Conclusions

In conclusion, using network pharmacology, molecular docking, molecular dynamics simulations, SPR analysis, and in vitro experiments, this study showed that Dp attenuates LPS-induced inflammatory responses in RAW264.7 cells, with evidence supporting the involvement of the PI3K/Akt/NF-κB signaling pathway. SPR analysis provided direct biophysical evidence of binding between Dp and AKT1 under the assay conditions. These findings provide mechanistic insights into the anti-inflammatory effects of Dp in macrophages and support further investigation of its potential relevance to vascular disease.

Author Contributions: Conceptualization, Y.Z. and D.Y.; methodology, Y.Z., L.F., H.L. and D.Y.; validation, Y.Z., H.L. and L.Y.; formal analysis, Y.Z. and H.L.; investigation, Y.Z., L.F. and S.J.; resources, D.Y.; data curation, Y.Z., L.F. and H.L.; writing—original draft preparation, Y.Z.; writing—review and editing, Y.Z., T.Z. and D.Y.; visualization, Y.Z., L.Y. and T.Z.; supervision, D.Y.; project administration, D.Y.; funding acquisition, D.Y. All authors have read and agreed to the published version of the manuscript.

Funding: This research was funded by the National Natural Science Foundation of China (grant number 82474115), the Natural Science Foundation of Hunan Province (grant number 2025JJ90080), the Hunan Provincial Department of Education (grant number 25C0235), the Hunan Provincial Administration of Traditional Chinese Medicine (grant number B20260015), the National Innovation Training Program for College Students (grant number 202510541026), and the Undergraduate Innovation Training Program of Hunan University of Chinese Medicine (grant number X202610541261).

Institutional Review Board Statement: Not applicable.

Informed Consent Statement: Not applicable.

Data Availability Statement: Data will be made available on request.

Conflicts of Interest: The authors declare that they have no known competing financial interests or personal relationships that could have appeared to influence the work reported in this paper.

Abbreviations

The following abbreviations are used in this manuscript:

Dp	Delphinidin
AS	Atherosclerosis
RMSD	Root-mean-square deviation
RMSF	Root-mean-square fluctuation
SASA	Solvent-accessible surface area
Rg	Radius of gyration
TCM	Traditional Chinese medicine
TTD	Therapeutic Target Database
COX-2	Cyclooxygenase-2
DMEM	Dulbecco's modified Eagle medium
GO	Gene Ontology
KEGG	Kyoto Encyclopedia of Genes and Genomes
LPS	Lipopolysaccharide
NF-κB	Nuclear factor kappa-B
OMIM	Online Mendelian Inheritance in Man
oxLDL	Oxidized low-density lipoprotein
PI3K	Phosphatidylinositol 3-kinase
Akt	Protein kinase B
SMILES	Simplified Molecular Input Line Entry System
STRING	Search Tool for the Retrieval of Interacting Genes/Proteins
DAVID	Database for Annotation, Visualization and Integrated Discovery
iNOS	Inducible nitric oxide synthase
IL-1β	Interleukin-1 beta
IL-6	Interleukin-6
TNF-α	Tumor necrosis factor-alpha
SPR	Surface plasmon resonance

References

1. Chen, R.; Zhang, H.; Tang, B.; Luo, Y.; Yang, Y.; Zhong, X.; Chen, S.; Xu, X.; Huang, S.; Liu, C. Macrophages in cardiovascular diseases: Molecular mechanisms and therapeutic targets. *Signal Transduct. Target. Ther.* **2024**, *9*, 130. [CrossRef] [PubMed]
2. Björkegren, J.; Lusis, A.J. Atherosclerosis: Recent developments. *Cell* **2022**, *185*, 1630–1645. [CrossRef] [PubMed]
3. Ajoolabady, A.; Pratico, D.; Lin, L.; Mantzoros, C.S.; Bahijri, S.; Tuomilehto, J.; Ren, J. Inflammation in atherosclerosis: Pathophysiology and mechanisms. *Cell Death Dis.* **2024**, *15*, 817. [CrossRef] [PubMed]
4. Traeuble, K.; Munz, M.; Pauli, J.; Sachs, N.; Vafadarnejad, E.; Carrillo-Roa, T.; Maegdefessel, L.; Kastner, P.; Heinig, M. Integrated single-cell atlas of human atherosclerotic plaques. *Nat. Commun.* **2025**, *16*, 8255. [CrossRef] [PubMed]
5. Dib, L.; Koneva, L.A.; Edsfeldt, A.; Zurke, Y.X.; Sun, J.; Nitulescu, M.; Attar, M.; Lutgens, E.; Schmidt, S.; Lindholm, M.W.; et al. Lipid-associated macrophages transition to an inflammatory state in human atherosclerosis increasing the risk of cerebrovascular complications. *Nat. Cardiovasc. Res.* **2023**, *2*, 656–672. Erratum in *Nat Cardiovasc Res.* **2023**, *2*, 794. https://doi.org/10.1038/s44161-023-00319-6. [CrossRef] [PubMed]

6. Ridker, P.M.; Bhatt, D.L.; Pradhan, A.D.; Glynn, R.J.; MacFadyen, J.G.; Nissen, S.E.; on behalf of the PROMINENT, REDUCE-IT, and STRENGTH Investigators. Inflammation and cholesterol as predictors of cardiovascular events among patients receiving statin therapy: A collaborative analysis of three randomised trials. *Lancet* **2023**, *401*, 1293–1301. [CrossRef] [PubMed]
7. Writing Committee Members; Virani, S.S.; Newby, L.K.; Arnold, S.V.; Bittner, V.; Brewer, L.C.; Demeter, S.H.; Dixon, D.L.; Fearon, W.F.; Hess, B.; et al. 2023 AHA/ACC/ACCP/ASPC/NLA/PCNA Guideline for the Management of Patients With Chronic Coronary Disease: A Report of the American Heart Association/American College of Cardiology Joint Committee on Clinical Practice Guidelines. *J. Am. Coll. Cardiol.* **2023**, *82*, 833–955. Erratum in *Circulation* **2023**, *148*, e186. https://doi.org/10.1161/CIR.0000000000001195. [CrossRef] [PubMed]
8. Monaco, C.; McNamara, C.A.; Slütter, B.; Foks, A.C.; Bekiranov, S.; Mulder, W.; Goncalves, I.; Lutgens, E.; on behalf of the LeDucq International Network of Excellence on Immune Checkpoints in Atherosclerosis: "CHECKPOINT ATHERO". Immunotherapy for atherosclerosis. *Physiol. Rev.* **2025**, *105*, 2141–2230. [CrossRef] [PubMed]
9. Dai, Z.; Huang, W.; Xiao, C.; You, F.; Long, J. Macrophages in post-chemoradiotherapy hematopoietic injury: A double-edged sword. *Cell Commun. Signal.* **2026**, *24*, 166. [CrossRef] [PubMed]
10. Nijat, D.; Zhao, Q.; Abdurixit, G.; He, J.; Liu, H.; Li, J. An Up-to-Date Review of Traditional Chinese Medicine in the Treatment of Atherosclerosis: Components, Mechanisms, and Therapeutic Potentials. *Phytother. Res.* **2025**, *39*, 3709–3735. [CrossRef] [PubMed]
11. Zheng, Y.; Chen, K.; Zhang, S.; Jing, J.; Zhou, Z.; Lu, J.; Holscher, C.; Chen, W.; Li, L. A food-medicine homology formulation ameliorates atherosclerosis by attenuating dyslipidemia and inflammation via the PI3K/Akt/NF-κB pathway. *Front. Pharmacol.* **2025**, *16*, 1710585. [CrossRef] [PubMed]
12. Casagrande, J.G.; Rogero, M.M.; de Oliveira, D.C.; Quintanilha, B.J.; Capetini, V.C.; Makiyama, E.N.; Neves, B.; da Silva Gonçalves, C.E.; de Freitas, S.; Hassimotto, N.; et al. Effects of grape juice intake on the cell migration properties in overweight women: Modulation mechanisms of cell migration in vitro by delphinidin-3-O-glucoside. *Food Res. Int.* **2024**, *178*, 113873. [CrossRef] [PubMed]
13. Bhattacharjee, S.; Dashwood, R.H. Epigenetic Regulation of NRF2/KEAP1 by Phytochemicals. *Antioxidants* **2020**, *9*, 865. [CrossRef] [PubMed]
14. Lu, J.; Tang, Y.; Li, H.; Tian, S.; Chen, X.; Song, X.; Qin, P.; Xu, J.; Zhu, H.; Ni, L.; et al. Exploring anti-SARS-CoV-2 natural products: Dual-viral target inhibition by delphinidin and the anti-coronaviral efficacy of deapio platycodin D. *Nat. Prod. Bioprospect* **2025**, *15*, 39. [CrossRef] [PubMed]
15. Xiang, J.J.; Chen, N.; Li, H.; Zhang, X.; Yang, B.; Huang, L.Q. [Analysis of flavonoids from saffron floral bio-residues]. *J. Chin. Mater. Medica* **2021**, *46*, 1438–1449. [CrossRef] [PubMed]
16. He, M.; Zhang, G.; Huo, D.; Yang, S. Combined Metabolome and Transcriptome Analysis of Creamy Yellow and Purple Colored Panax notoginseng Roots. *Life* **2023**, *13*, 2100. [CrossRef] [PubMed]
17. Xu, Y.; Jin, B.; Yin, P.; Cheng, K.; Li, Q.; Ding, H. Targeting cancer with delphinidin: From molecular insights to therapeutic implications. *Front. Pharmacol.* **2026**, *17*, 1778570. [CrossRef] [PubMed]
18. Kwon, J.Y.; Lee, K.W.; Kim, J.E.; Jung, S.K.; Kang, N.J.; Hwang, M.K.; Heo, Y.S.; Bode, A.M.; Dong, Z.; Lee, H.J. Delphinidin suppresses ultraviolet B-induced cyclooxygenases-2 expression through inhibition of MAPKK4 and PI-3 kinase. *Carcinogenesis* **2009**, *30*, 1932–1940. [CrossRef] [PubMed]
19. Walker, E.H.; Pacold, M.E.; Perisic, O.; Stephens, L.; Hawkins, P.T.; Wymann, M.P.; Williams, R.L. Structural determinants of phosphoinositide 3-kinase inhibition by wortmannin, LY294002, quercetin, myricetin, and staurosporine. *Mol. Cell* **2000**, *6*, 909–919. [CrossRef] [PubMed]
20. Martis, E.; Téletchéa, S. Ten quick tips to perform meaningful and reproducible molecular docking calculations. *PLoS Comput. Biol.* **2025**, *21*, e1013030. [CrossRef] [PubMed]
21. Nogales, C.; Mamdouh, Z.M.; List, M.; Kiel, C.; Casas, A.I.; Schmidt, H. Network pharmacology: Curing causal mechanisms instead of treating symptoms. *Trends Pharmacol. Sci.* **2022**, *43*, 136–150. [CrossRef] [PubMed]
22. Basu, A.; Sarkar, A.; Maulik, U. Molecular docking study of potential phytochemicals and their effects on the complex of SARS-CoV2 spike protein and human ACE2. *Sci. Rep.* **2020**, *10*, 17699. [CrossRef] [PubMed]
23. Li, S.; He, J.; Hu, H.; Wang, G.; Tang, J.; Yao, J.; Shen, J.; Li, X. Unraveling anti-atherosclerosis mechanism of anthocyanins from Xinjiang wild cherry plum (Prunus divaricata Ledeb) via network pharmacology and molecular docking. *Bioresour. Bioprocess.* **2025**, *12*, 53. [CrossRef] [PubMed]
24. Hou, D.X.; Yanagita, T.; Uto, T.; Masuzaki, S.; Fujii, M. Anthocyanidins inhibit cyclooxygenase-2 expression in LPS-evoked macrophages: Structure-activity relationship and molecular mechanisms involved. *Biochem. Pharmacol.* **2005**, *70*, 417–425. [CrossRef] [PubMed]
25. Haseeb, A.; Chen, D.; Haqqi, T.M. Delphinidin inhibits IL-1β-induced activation of NF-κB by modulating the phosphorylation of IRAK-1(Ser376) in human articular chondrocytes. *Rheumatology* **2013**, *52*, 998–1008. [CrossRef] [PubMed]
26. Neves, B.; de Freitas, S.; Borelli, P.; Rogero, M.M.; Fock, R.A. Delphinidin-3-O-glucoside in vitro suppresses NF-κB and changes the secretome of mesenchymal stem cells affecting macrophage activation. *Nutrition* **2023**, *105*, 111853. [CrossRef] [PubMed]

27. Xu, J.; Hao, P.; Chen, J.; Mai, D.; Wang, Y.; Chen, R.; Yang, J.; Li, R.; Xing, X.; Yan, Z.; et al. Delphinidin-3-O-glucoside attenuates neonatal hypoxic-ischemic encephalopathy in a neonatal mouse model by reprogramming microglial polarization. *Front. Pharmacol.* **2026**, *17*, 1797078. [CrossRef] [PubMed]
28. Liu, Y.; Hong, T.; Lv, M.; Guo, X.; Zhang, P.; Yan, A.; Wei, W. Delphinidin attenuates cognitive deficits and pathology of Alzheimer's disease by preventing microglial senescence via AMPK/SIRT1 pathway. *Alzheimer's Res. Ther.* **2025**, *17*, 138. [CrossRef] [PubMed]
29. Jin, X.; Yi, L.; Chen, M.L.; Chen, C.Y.; Chang, H.; Zhang, T.; Wang, L.; Zhu, J.D.; Zhang, Q.Y.; Mi, M.T. Delphinidin-3-glucoside protects against oxidized low-density lipoprotein-induced mitochondrial dysfunction in vascular endothelial cells via the sodium-dependent glucose transporter SGLT1. *PLoS. ONE* **2013**, *8*, e68617, Correction in *PLOS ONE* **2014**, *9*. https://doi.org/10.1371/annotation/774b483b-cba3-46ce-a922-09d7f05487b0. [CrossRef] [PubMed]
30. Martin, S.; Giannone, G.; Andriantsitohaina, R.; Martinez, M.C. Delphinidin, an active compound of red wine, inhibits endothelial cell apoptosis via nitric oxide pathway and regulation of calcium homeostasis. *Br. J. Pharmacol.* **2003**, *139*, 1095–1102. [CrossRef] [PubMed]
31. Lai, X.; Li, X.; Chen, J.; Liu, X.; Pan, P.; Zhou, Y.; Zhao, G. Advances in flavonoid glycosylation: Chemical and biological basis, mechanisms, physicochemical properties, and applications in the food industry. *Trends Food Sci. Technol.* **2025**, *165*, 105296. [CrossRef]
32. Baumer, Y.; Irei, J.; Boisvert, W.A. Cholesterol crystals in the pathogenesis of atherosclerosis. *Nat. Rev. Cardiol.* **2025**, *22*, 315–332. [CrossRef] [PubMed]
33. Zhu, L.; Chen, Q.; Wang, B.; Fu, J.; Liu, Z.; Cui, Y.; Zhang, R.; Liu, F.; Niu, S.; Zhou, Y. PI3K/AKT signaling pathway: New strategies for treating atherosclerosis with plant-derived compounds. *Front. Pharmacol.* **2026**, *17*, 1722493. [CrossRef] [PubMed]
34. Li, M.; Wu, L.; Wen, Y.; Wang, A.; Zhou, X.; Ren, L.; Lu, Q.; Li, F.; Zhu, L.; Tang, C. Dysregulated cholesterol uptake and efflux of bone marrow-derived α-SMA(+) macrophages contribute to atherosclerotic plaque formation. *Cell. Mol. Life Sci.* **2025**, *82*, 134. [CrossRef] [PubMed]
35. Fougerat, A.; Gayral, S.; Gourdy, P.; Schambourg, A.; Rückle, T.; Schwarz, M.K.; Rommel, C.; Hirsch, E.; Arnal, J.F.; Salles, J.P.; et al. Genetic and pharmacological targeting of phosphoinositide 3-kinase-gamma reduces atherosclerosis and favors plaque stability by modulating inflammatory processes. *Circulation* **2008**, *117*, 1310–1317. [CrossRef] [PubMed]
36. Wang, J.; Bai, X.; Song, Q.; Fan, F.; Hu, Z.; Cheng, G.; Zhang, Y. *miR*-223 Inhibits Lipid Deposition and Inflammation by Suppressing Toll-Like Receptor 4 Signaling in Macrophages. *Int. J. Mol. Sci.* **2015**, *16*, 24965–24982. [CrossRef] [PubMed]
37. Arranz, A.; Doxaki, C.; Vergadi, E.; Martinez de la Torre, Y.; Vaporidi, K.; Lagoudaki, E.D.; Ieronymaki, E.; Androulidaki, A.; Venihaki, M.; Margioris, A.N.; et al. Akt1 and Akt2 protein kinases differentially contribute to macrophage polarization. *Proc. Natl. Acad. Sci. USA* **2012**, *109*, 9517–9522. [CrossRef] [PubMed]
38. Gharbi, S.I.; Zvelebil, M.J.; Shuttleworth, S.J.; Hancox, T.; Saghir, N.; Timms, J.F.; Waterfield, M.D. Exploring the specificity of the PI3K family inhibitor LY294002. *Biochem. J.* **2007**, *404*, 15–21. [CrossRef] [PubMed]
39. Bae, C.H.; Jeon, B.S.; Choi, Y.S.; Song, S.Y.; Kim, Y.D. Delphinidin Inhibits LPS-Induced MUC8 and MUC5B Expression Through Toll-like Receptor 4-Mediated ERK1/2 and p38 MAPK in Human Airway Epithelial Cells. *Clin. Exp. Otorhinolaryngol.* **2014**, *7*, 198–204. [CrossRef] [PubMed]
40. Hidalgo, A.I.; Vega, M.; Maldonado, D.; Teuber, S.; Burgos, R.A.; Hidalgo, M.A. Delphinidin Exerts Immunomodulatory Effects in Canine Neutrophils and Peripheral Blood Mononuclear Cells by Limiting Tissue Damaging Mechanisms and Regulating Cytokine Responses. *Animals* **2026**, *16*, 746. [CrossRef] [PubMed]
41. Matsumoto, H.; Inaba, H.; Kishi, M.; Tominaga, S.; Hirayama, M.; Tsuda, T. Orally administered delphinidin 3-rutinoside and cyanidin 3-rutinoside are directly absorbed in rats and humans and appear in the blood as the intact forms. *J. Agric. Food Chem.* **2001**, *49*, 1546–1551. [CrossRef] [PubMed]
42. Grotemeyer, A.; Alexander, S.; Frieß, L.; Roewer, J.; Bankoglu, E.E.; Badr, M.; Wu, J.; Stopper, H.; Volkmann, J.; Roewer, N.; et al. Delphinidin modulates neuroinflammation and behavioral deficits in a Parkinson's disease mouse model. *npj Park. Dis.* **2026**, *12*, 32. [CrossRef] [PubMed]
43. Husain, A.; Chanana, H.; Khan, S.A.; Dhanalekshmi, U.M.; Ali, M.; Alghamdi, A.A.; Ahmad, A. Chemistry and Pharmacological Actions of Delphinidin, a Dietary Purple Pigment in Anthocyanidin and Anthocyanin Forms. *Front. Nutr.* **2022**, *9*, 746881. [CrossRef] [PubMed]
44. Goszcz, K.; Deakin, S.J.; Duthie, G.G.; Stewart, D.; Megson, I.L. Bioavailable Concentrations of Delphinidin and Its Metabolite, Gallic Acid, Induce Antioxidant Protection Associated with Increased Intracellular Glutathione in Cultured Endothelial Cells. *Oxid. Med. Cell. Longev.* **2017**, *2017*, 9260701. [CrossRef] [PubMed]
45. Cheng, Y.; Liu, J.; Li, L.; Ren, J.; Lu, J.; Luo, F. Advances in embedding techniques of anthocyanins: Improving stability, bioactivity and bioavailability. *Food Chem. X* **2023**, *20*, 100983. [CrossRef] [PubMed]
46. Barkallah, M.; Nzoughet-Kouassi, J.; Simard, G.; Thoulouze, L.; Marze, S.; Ropers, M.H.; Andriantsitohaina, R. Enhancement of the Anti-Angiogenic Effects of Delphinidin When Encapsulated within Small Extracellular Vesicles. *Nutrients* **2021**, *13*, 4378. [CrossRef] [PubMed]

47. Berman, H.M.; Westbrook, J.; Feng, Z.; Gilliland, G.; Bhat, T.N.; Weissig, H.; Shindyalov, I.N.; Bourne, P.E. The Protein Data Bank. *Nucleic Acids Res.* **2000**, *28*, 235–242. [CrossRef] [PubMed]
48. Morris, G.M.; Huey, R.; Lindstrom, W.; Sanner, M.F.; Belew, R.K.; Goodsell, D.S.; Olson, A.J. AutoDock4 and AutoDockTools4: Automated docking with selective receptor flexibility. *J. Comput. Chem.* **2009**, *30*, 2785–2791. [CrossRef] [PubMed]
49. Trott, O.; Olson, A.J. AutoDock Vina: Improving the speed and accuracy of docking with a new scoring function, efficient optimization, and multithreading. *J. Comput. Chem.* **2010**, *31*, 455–461. [CrossRef] [PubMed]

Disclaimer/Publisher's Note: The statements, opinions and data contained in all publications are solely those of the individual author(s) and contributor(s) and not of MDPI and/or the editor(s). MDPI and/or the editor(s) disclaim responsibility for any injury to people or property resulting from any ideas, methods, instructions or products referred to in the content.